JGR Solid Earth

RESEARCH ARTICLE
10.1029/2019JB017417

The Mechanism of Methane Gas Migration Through the Gas Hydrate Stability Zone: Insights From Numerical Simulations

Jinlong Liu[1,2,3], Matthias Haeckel[3], Jonny Rutqvist[4], Shuhong Wang[1], and Wen Yan[1,2]

[1]CAS Key Laboratory of Ocean and Marginal Sea Geology, South China Sea Institute of Oceanology, Chinese Academy of Sciences, Guangzhou, China, [2]College of Earth and Planetary Sciences, University of Chinese Academy of Sciences, Beijing, China, [3]GEOMAR Helmholtz Centre for Ocean Research Kiel, Kiel, Germany, [4]Lawrence Berkeley National Laboratory, Berkeley, CA, USA

Key Points:
- Free gas can migrate through the GHSZ if it is supplied in excess of the consumption by gas hydrate formation
- Effective gas transport through the GHSZ requires a high gas supply as it is possible in seismic pipe or chimney structures and faults
- Observed salinity peaks and temperatures are a result of intermittent high gas fluxes following overpressure buildup and fracturing

Correspondence to:
S. Wang and W. Yan,
wshds@scsio.ac.cn;
wyan@scsio.ac.cn

Citation:
Liu, J., Haeckel, M., Rutqvist, J., Wang, S., & Yan, W. (2019). The mechanism of methane gas migration through the gas hydrate stability zone: Insights from numerical simulations. *Journal of Geophysical Research: Solid Earth*, *124*, 4399–4427. https://doi.org/10.1029/2019JB017417

Received 21 JAN 2019
Accepted 23 APR 2019
Accepted article online 29 APR 2019
Published online 27 MAY 2019

Abstract Free gas migration through the gas hydrate stability zone (GHSZ) and subsequent gas seepage at the seabed are characteristic features in marine gas hydrate provinces worldwide. The biogenic or thermogenic gas is typically transported along faults from deeper sediment strata to the GHSZ. Several mechanisms have been proposed to explain free gas transport through the GHSZ. While inhibition of hydrate formation by elevated salinities and temperatures have been addressed previously in studies simulating unfocused, area-wide upward advection of gas, which is not adequately supported by field observations, the role of focused gas flow through chimney-like structures has been underappreciated in this context. Our simulations suggest that gas migration through the GHSZ is, fundamentally, a result of methane gas supply in excess of its consumption by hydrate formation. The required high gas flux is driven by local overpressure, built up from gas accumulating below the base of the GHSZ that fractures the overburden when exceeding a critical pressure, thereby creating the chimney-like migration pathway. Initially rapid hydrate formation raises the temperature in the chimney structure, thereby facilitating further gas transport through the GHSZ. As a consequence, high hydrate saturations form preferentially close to the seafloor, where temperatures drop to bottom water values, producing a prominent subsurface salinity peak. Over time, hydrates form at a lower rate throughout the chimney structure, while initial temperature elevation and salinity peak dissipate. Thus, our simulations suggest that the near-surface salinity peak and elevated temperatures are a result of transient high-flux gas migration through the GHSZ.

1. Introduction

Gaseous methane migration through the gas hydrate stability zone (GHSZ) has been observed in various geological settings along tectonically active (e.g., Heeschen et al., 2003; Kannberg et al., 2013; Klaucke et al., 2006; Law et al., 2010; Suess et al., 1999) and passive (e.g., Bünz et al., 2012; Smith, Mienert, et al., 2014) continental margins. At the seafloor the seeping methane gas sustains a rich ecosystem of chemosynthetic communities (Olu et al., 1997) and gives rise to the development of distinct seafloor features like authigenic carbonate rocks (Kulm et al., 1986), pockmarks (Hovland et al., 2005), or seafloor doming (Koch et al., 2015). Invasion of free gas into the shallow subsurface sediments could elevate gas pressure and reduce the shear strength of sediments, thereby triggering seafloor instabilities, such as submarine landslides (Locat & Lee, 2002; Whelan et al., 1977). In addition, methane emission into the ocean is an important process in the global carbon cycle (Dickens, 2003).

Free gas migration through the GHSZ has been considered enigmatic because intuitively the migrating gas should be converted into gas hydrate within the GHSZ or be trapped at the base of the gas hydrate stability zone (BGHSZ). Three groups of mechanisms to explain this enigma have been proposed. The first one refers to the upward advection of warm and/or saline fluids that shift the GHSZ close to the seafloor. While this has been documented in numerous instances at mud volcanoes or cold vents located above salt diapirs (e.g., Reitz et al., 2007; Ruppel et al., 2005; Wallmann et al., 2006), it does not serve as a general mechanism. We will therefore not consider this case in our study. Another group involves factors that suppress the kinetic rate of methane hydrate formation or affect its thermodynamic stability. In previous studies, the following factors have been discussed: limited availability of water in the pore space compared to the gas supply during hydrate formation (Clennell et al., 1999; Ginsburg & Soloviev, 1997; Liu & Flemings, 2006), locally

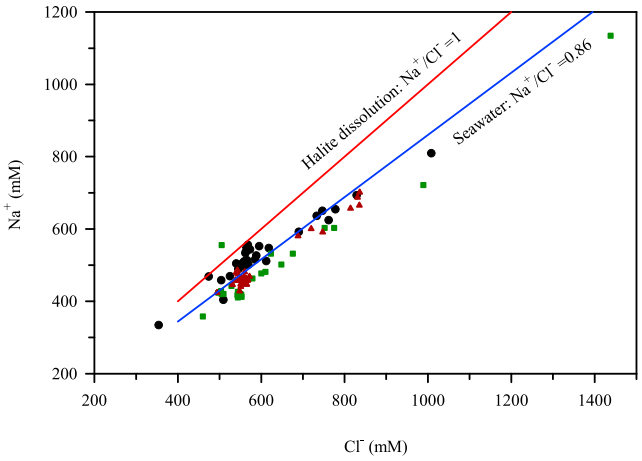

Figure 1. Observed pore water Na/Cl ratios at ODP Site 1249 (black circles) at southern Hydrate Ridge (Tréhu et al., 2003), Site UBGH2-3 (green squares) in the Ulleung Basin (Kim et al., 2013), and IODP Site U1328 (red triangles) at Cascadia Margin (Riedel et al., 2006).

elevated pore water salinity due to salt exclusion during hydrate formation (e.g., Liu & Flemings, 2006; Milkov et al., 2004), local heat release resulting from the exothermic hydrate formation (Garg et al., 2008; Smith, Flemings, et al., 2014), and capillary inhibition of hydrate formation (Clennell et al., 1999; Liu & Flemings, 2011). The third group focuses on excess supply of gaseous methane, that is, a higher transport rate relative to the rate of gas hydrate formation (Haeckel et al., 2004; Torres et al., 2004; Tréhu, Flemings, et al., 2004). However, evidence from field data for the latter two groups of mechanisms is scarce.

Elevated pore water salinity owing to hydrate formation has been described only for three scientific drill sites, ODP Site 1249 at southern Hydrate Ridge (Tréhu et al., 2003), Site UBGH2-3 in the Ulleung Basin offshore Korea (Kim et al., 2013), and the Bullseye vent IODP Site U1328 at Cascadia Margin (Riedel et al., 2006). Consequently, at all three sites Na/Cl ratios are close to the seawater value of 0.86 (Figure 1), hence ruling out diapiric influences as documented in other areas, such as Garden Banks lease blocks GB424/425 and Ursa Vent in lease blocks MC852/853 in the northern Gulf of Mexico (Castellini et al., 2006; Ruppel et al., 2005) as well as ODP Site 996 at Blake Ridge (Paull et al., 1996). Increased salinity can inhibit hydrate formation; however, observed maximum salinities at the three sites are all well below concentrations that are needed to induce three-phase equilibrium conditions sufficiently inhibiting gas hydrate formation (Figure 2). In addition, the salt enrichments only occur in the uppermost tens of meters below the seafloor and not throughout the GHSZ. At ODP Site 1249, Milkov et al. (2005) explained this absence of high salinity by lateral migration of free gas due to a deflection by the less-permeable carbonate and gas hydrate caps near the seafloor at the Pinnacle (Figure 3). However, at Site 1250, located at the proposed lateral pathway no significant salinity enrichment has been observed (Tréhu et al., 2003), and evidence for such lateral gas migration is also missing at the other two locations, Site UBGH2-3 and Site U1328. At Bullseye vent IODP Site U1328 on the Cascadia accretionary prism (Riedel et al., 2006) salinities are elevated only moderately, thus being quite far from effectively inhibiting gas hydrate formation (Figure 2).

Despite the moderate to high-salinity peaks, no temperature elevations have been reported at ODP Site 1249 and IODP Site U1328 (Figure 4; no data published for Site UBGH2-3) as it would be expected in the course of the exothermic near-surface hydrate formation. While this may be explained by fast dissipation of the released heat as previous numerical modeling studies (Garg et al., 2008; Smith, Flemings, et al., 2014)

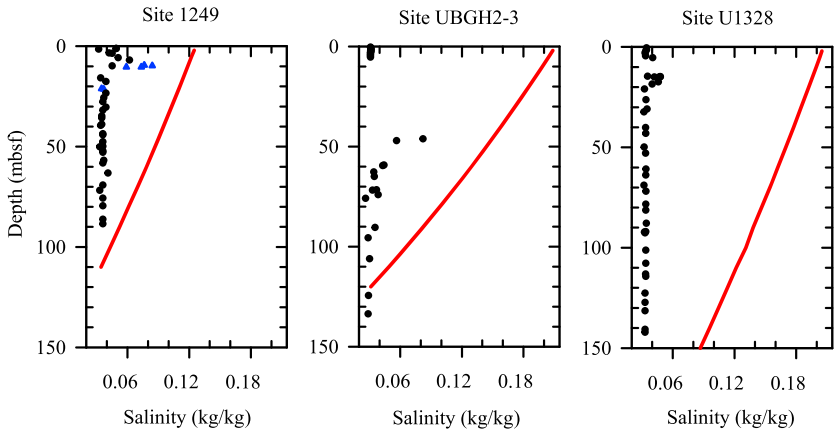

Figure 2. Comparison of measured salinity (black circles) from whole-round sediment samples and calculated three-phase equilibrium curve (red line) at ODP Site 1249 at southern Hydrate Ridge (Tréhu et al., 2003), Site UBGH2-3 in the Ulleung basin (Kim et al., 2013), and IODP Site U1328 at Cascadia Margin (Riedel et al., 2006). Blue triangles of ODP Site 1249 represent salinities measured in dry-looking sediment, not disturbed by shipboard gas hydrate dissociation (Torres et al., 2004).

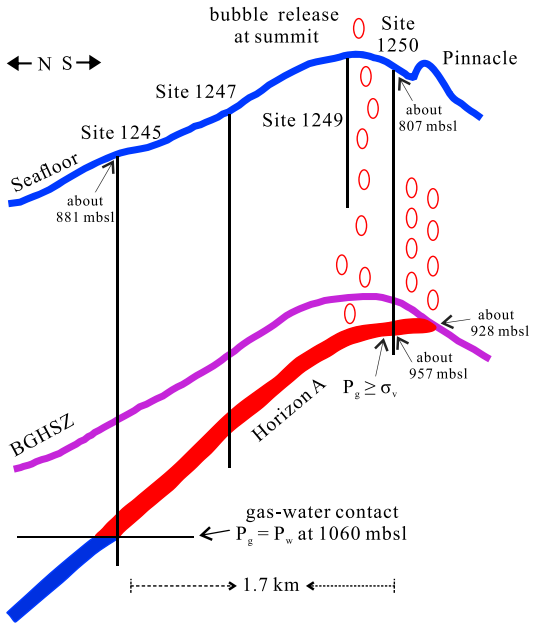

Figure 3. Conceptual model of the gas hydrate system at the southern Hydrate Ridge, modified from Tréhu, Flemings, et al. (2004). Please note that there is no horizontal and vertical scale, and the relative location of Sites 1245, 1249, and 1250 is approximate.

suggested that considered the coupled role of heat production and salt exclusion for passing free gas through the GHSZ, these simulations produced elevated salinities throughout the GHSZ. Thus, the observed combination of "normal" temperature profile and near-surface salinity peak (Figures 2 and 4) has not been explained in a consistent way so far.

Using core log and sediment data, Tréhu, Flemings, et al. (2004) showed that at southern Hydrate Ridge, gas pressures beneath the BGHSZ are high enough to trigger hydraulic fracturing (Figure 3) and that the focused fluid flow after fracturing can provide methane to the GHSZ in excess of the methane proportion in gas hydrate, resulting in free gas transport through the GHSZ. Based on a 3-D high-resolution seismic data analysis offshore Vancouver Island, Zühlsdorff and Spiess (2004) also suggested that hydraulic fracturing is an efficient process to create permeable pathways that allow for methane ebullition through the seabed. Daigle et al. (2011) suggested that any modeling work trying to explain how free gas migrates through the GHSZ should combine focused fluid flow induced by hydrofracturing and the thermodynamic inhibition of gas hydrate formation. Nevertheless, this has not been attempted until now.

Consequently, in this paper, we present two-dimensional numerical simulations considering focused fluid flow through vertical chimney structures caused by overpressure-induced hydraulic fracturing and the potential self-inhibition of gas hydrate formation by the produced salinity and temperature increases in order to investigate the dynamics that allow free gas to migrate through the GHSZ. We use the situation at southern Hydrate Ridge as case study, because this site shows the most pronounced salinity enrichment and has been studied previously more comprehensively than Cascadia margin and the Ulleung basin. Our simulations reveal the dynamic interplay and sequence of the various transport and reaction processes that are fundamental for free gas migration through the GHSZ, thereby successfully reproducing the salinity and temperature data of ODP Site 1249.

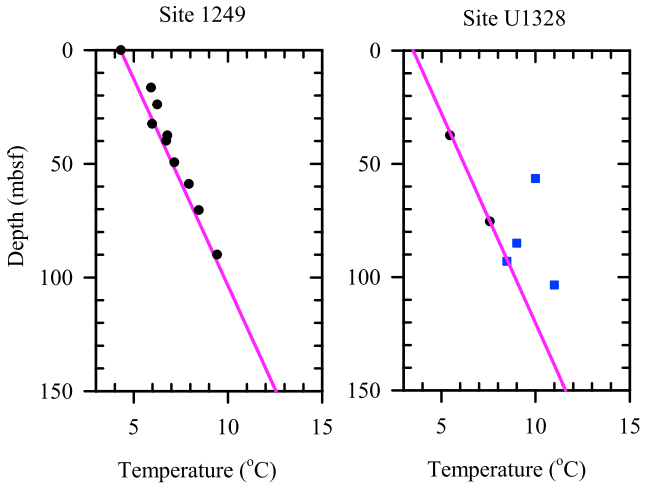

Figure 4. Measured temperature values (black circles) and fitted geothermal gradient (red lines) at ODP Site 1249 (Garg et al., 2008; Torres et al., 2004; Tréhu et al., 2003) and IODP Site U1328 (Riedel et al., 2006). The temperature values indicated by the blue squares at IODP Site U1328 have been marked as being unreliable by Riedel et al. (2006).

2. Model Details

Numerical simulations were conducted using a modified TOUGH +HYDRATE code (Moridis et al., 2008) by implementing the kinetic expression for hydrate formation suggested by Li et al. (2014) and intrinsic permeability parameterizations for hydraulically fractured flow pathways.

2.1. Kinetics of Gas Hydrate Dissociation and Formation

In TOUGH+HYDRATE, gas hydrate dissociation is assumed to occur on the surface of hydrate particles that are uniformly distributed within the interstitial spaces of the porous medium, and the surface area A involved in the reaction is calculated to be proportional to the hydrate saturation with the power 2/3, that is, $A \sim S_h^{2/3}$ (Moridis et al., 2008). However, during hydrate formation the gas consumption rate is predominantly controlled by the mass transfer across the gas-liquid contact area (Mohebbi et al., 2012; Skovborg & Rasmussen, 1994). Hence, the surface area (per m^3) of the gas-water interface is expressed by (Li et al., 2014)

$$A = N_V\left(4\pi r_P^2\right) S_g^{2/3} S_a^{2/3} (1-S_h)^{2/3} \quad (1)$$

where S_g, S_a, and S_h are the volumetric saturations of free gas, pore water, and gas hydrate, respectively. The sediment grains are considered to be spherical particles, and r_P is the solid grain radius in m. N_V is the

number of interstitial pore spaces in a unit volume of bulk sediment, and N_V is assumed to be equal to the number of solid grains, $\frac{1-\phi_0}{4\pi r_P^3/3}$ (Moridis et al., 2008). Based on this assumption, the volume of each pore space V_V, equal to $\frac{4}{3}\pi r_P^3 \frac{\phi_0}{1-\phi_0}$, is related to the grain radius r_P. Parameter ϕ_0 is the porosity. More details about the derivation of equation (1) can be found in Li et al. (2014).

Therefore, the original equation in TOUGH+HYDRATE was replaced by the respective model and parameterization of Li et al. (2014):

$$R_M = K_0 \exp(-\Delta E_a/RT) A \left(f_g - f_{eq}\right) \frac{M_{\mathrm{CH_4}}}{M_{\mathrm{Hyd}}} \tag{2}$$

where R_M is the methane consumption or release rate due to hydrate reaction in kg m^{-3} s^{-1}, $K_0 = 8.06$ kg m^{-2} Pa^{-1} s^{-1} is the intrinsic hydrate reaction constant for both formation and dissociation, ΔE_a is the hydrate activation energy of 8.09×10^4 J/mol, R is the universal gas constant of 8.314 J mol^{-1} K^{-1}, T is the absolute temperature in K, f_{eq} is the gas fugacity in Pa at thermodynamic equilibrium of methane hydrate for a given temperature T, f_g is the actual gas fugacity in Pa at that temperature, $M_{\mathrm{CH_4}}$ is the molecular weight of CH_4 in kg/mol, and M_{Hyd} is the molecular weight of hydrate in kg/mol. For $f_g \geq f_{eq}$, indicating hydrate formation, we have $R_M \geq 0$ in equation (2), and we define $C_M = R_M$, where C_M is the methane consumption rate due to hydrate formation in kg m^{-3} s^{-1}. For $f_g < f_{eq}$, denoting hydrate dissociation, we have $R_M < 0$ in equation (2), and we define $D_M = -R_M$, where D_M is the methane release rate due to hydrate dissociation in kg m^{-3} s^{-1}. C_M and D_M are defined to facilitate the comparison of the methane consumption and release rate in the same plot and as positive values (for example in Figure 7e).

In our simulations we assume that methane gas dissolution into the pore water and exsolution out of the aqueous phase are sufficiently fast to instantly reach gas-liquid two-phase equilibrium. Thus, the fugacity coefficient of gaseous methane is computed from a Peng-Robinson equation of state, and the fugacity of dissolved methane f_d is assumed to be equal to the gaseous fugacity f_g. Three-phase equilibrium is typically achieved when f_g approaches f_{eq}, and $S_a > 0$, $S_h > 0$, and $S_g > 0$ at the same time.

The effect of salinity on hydrate formation is described by the standard option in TOUGH+HYDRATE (Moridis et al., 2008), while the hydrate reaction enthalpy, ΔH, is calculated according to the temperature-dependent equation of Kamath (1984)

$$\Delta H = 456.06 - 0.1356T \ (273.16K < T \leq 298.16K) \tag{3}$$

During our simulations, the temperature in the GHSZ ranges from 4.3 °C at seafloor to about 11.3 °C at the BGHSZ, therefore giving ΔH values of 417.4–418.4 kJ/kg within the GHSZ in our model. These values are slightly lower than the constant values of 421 and 450 kJ/kg used by Smith, Flemings, et al. (2014) and Garg et al. (2008), respectively. We believe that this discrepancy lies within the general uncertainty for gas hydrate systems.

2.2. Intrinsic Permeability of Fractured Sediments

The state of stress is assumed to be isotropic (i.e., the maximum principal stress is equal to the minimum principal stress) in our model domain. This assumption can be valid because of the chaotic fracture orientations within the GHSZ at our case study site, that is, the southern summit of Hydrate Ridge (Daigle et al., 2011; Weinberger & Brown, 2006). Seafloor horizontal stress might be slightly lower than the vertical stress; that is, horizontal stress would be the minimum stress favoring vertical hydraulic fractures (Reilly & Flemings, 2010). If stress is exactly isotropic as assumed here, the orientation of fracture initiation is not obvious; however, fracturing and failure would still propagate vertically because of the vertical stress gradient. We also assume that the sediment cohesion or tensile strength is zero, and the sediment strength increase due to the presence of hydrate was not considered in this study. The shallow part of the fine-grained marine sediments without hydrate typically has small cohesion and tensile strength (Behrmann, 1991; Daigle & Dugan, 2010a, 2010b). In our simulations, when the hydraulic fracturing starts to propagate from the BGHSZ and arrives at the seafloor, the hydrate saturation is low (generally less than 6%) except near the BGHSZ (i.e., the hydrate saturation is high only near the BGHSZ when the fracture network has been completely created). Therefore, the effect of hydrate on the sediment strength can be negligible within the zone

well above BGHSZ. An evident impact of this assumption is to moderately underestimate the time required to achieve the fracturing criterion near the BGHSZ because pore pressures should have to overcome additional sediment strength and cohesion (Daigle & Dugan, 2010a, 2010b).

Based on the aforementioned assumptions, in our simulations hydraulic fracturing is considered to initiate at the BGHSZ, if the pore pressure P_P at the BGHSZ exceeds the local overburden stress σ_v, which is calculated to be equal to the weight of the overlying water and sediment column. Then, the sediment above the BGHSZ is considered to be fractured, only when the local pore fluid pressure within the GHSZ has been elevated sufficiently and thereby exceeding the local overburden stress. Subsequent to fracturing at the BGHSZ, the high pore fluid pressure will propagate from the BGHSZ to the seafloor. Hence, in reality formation of a fracture network through the GHSZ will take some time and not occur instantaneously after the gas pressure has exceeded the overburden stress at the BGHSZ. However, since simulating of the actual fracturing process is out of scope of this study, we simply introduce a more permeable flow pathway in the 2-D model domain, once the above fracturing criterion is fulfilled. The intrinsic permeability in such a fracture can be estimated either by the discrete fracture or the continuum model.

In the discrete fracture model, each fracture is considered to be bound by two smooth, parallel walls having an aperture d, and fluid flow through the fracture is assumed to be laminar. The permeability of each fracture is (Snow, 1968; Zimmerman & Bodvarsson, 1996)

$$k_{\text{fracture}} = \frac{d^2}{12} \tag{4}$$

In the concept of the equivalent continuum model, a network of micro-fractures is treated as a continuous medium with uniform hydraulic properties representing the average effect of the individual fractures (Leung et al., 2012). Hence, the equivalent permeability can be understood to derive from the discrete fracture model, in which the network of micro-fractures is conceptualized as an explicit fracture. The equivalent volume of the fluid flowing through this discrete fracture is averaged over the inter-fracture spacing l, and therefore, the resulting equivalent permeability is (Daigle et al., 2011; Daigle & Dugan, 2011)

$$k_{ef} = \frac{d^3}{12l} \tag{5}$$

Assuming that the overpressure-induced hydraulic fracturing leads to a fracture network with values for d and l of 0.001 and 1 m, respectively (Daigle et al., 2011), the equivalent intrinsic permeability of the grid blocks in the model domain that achieve $P_P \geq \sigma_v$ is thus set to 8.3×10^{-11} m^2. The equivalent intrinsic permeability will be provided in both horizontal and vertical directions. In our work, this high intrinsic permeability within the fractured sediment will remain all the time once the sediment is fractured, even after the pressure drops below the local overburden stress.

2.3. Permeability Reduction Due to Hydrate Formation

TOUGH+HYDRATE calculates the effect of gas hydrate precipitating in the pore space on the intrinsic permeability by applying the modified Stone equation (Moridis et al., 2008; Stone, 1970):

$$k = k_{rS} k_i \tag{6}$$

$$k_{rS} = \left[\frac{\phi_0(1-S_h)-\phi_c}{\phi_0-\phi_c}\right]^{n_H} \tag{7}$$

where k_{rS} is the permeability adjustment factor due to the presence of gas hydrate in the intergranular space; k_i is the intrinsic permeability of the sediment without gas hydrate; ϕ_0 is the initial porosity of hydrate-free sediments; ϕ_c is the critical porosity, that is, the fraction of the pore space occupied by a small, residual amount of free gas; and n_H is a permeability reduction exponent due to hydrate formation.

Kossel et al. (2018) investigated experimentally the dependency of the water permeability on gas hydrate formation in quartz sand by measuring time-resolved maps of the three-dimensional gas hydrate saturation using nuclear magnetic resonance imaging, and then fitting a variety of permeability relationships to the

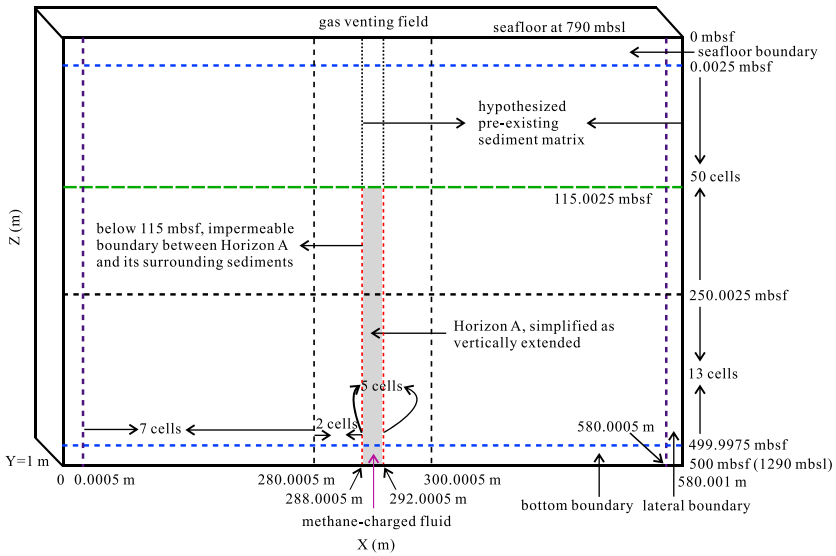

Figure 5. The geometry of the two-dimensional model domain applied for the simulation scenario at southern Hydrate Ridge. Note that the picture is not in scale.

experimental data applying 3-D finite element simulations. For the modified Stone equation (equation (7)) they reported fitted values of the exponent n_H of 11.4 for $\phi_c = 0$ and 10.8 for $\phi_c = 0.1$. In our simulation, we assume a critical porosity of $\phi_c = 0.01$ and a corresponding $n_H = 11.1$ to approximate the permeability reduction in the unfractured sediments.

For the fractured sediment, we apply a critical porosity ϕ_c of zero assuming that the fracture system has no percolation threshold. The changed fracture aperture arising from hydrate precipitation is considered to be (Nimblett & Ruppel, 2003)

$$d_h = d(1-S_h) \tag{8}$$

Then, according to equation (5), the intrinsic permeability of the fractured sediment after hydrate formation is

$$k_{ef\_h} = \frac{d_h^3}{12l} = \frac{[d(1-S_h)]^3}{12l} = \frac{d^3}{12l}(1-S_h)^3 = k_{ef}(1-S_h)^3 \tag{9}$$

Therefore, in comparison with equation (7) and considering $\phi_c = 0$ for the fractured sediment due to its zero percolation threshold, in the fractured chimney sediments we assume a lower exponent value of $n_H = 3$, thus obstructing flow less efficient than in the unfractured sediment. We expect that the chosen parameterization reflects the fracture dominant flow along preferentially oriented pore channels within which gas hydrates precipitate, and captures the essential trend of free gas migration through hydrate-charged fracture or fractured sediments.

2.4. Model Domain

In the model the free gas migration pathway (Horizon A at southern Hydrate Ridge) is simplified as being vertical and 4 m wide (Figure 5). The seafloor is idealized to be horizontal at 790 m below sea level (bsl), and the bottom boundary is set at 1,290 m bsl (i.e., 500m meters below seafloor (bsf)). The lateral extent of the model domain is ~580 m, located symmetrically on both sides of Horizon A. The BGHSZ depth is predicted to be 115 m bsf, inferred from an initial salinity of 0.03185 kg/kg (Torres et al., 2004), hydrostatic pressure (seafloor depth of 790 m bsl), and normal temperature (seafloor temperature of 4.3 °C (Garg et al., 2008) and initial geothermal gradient of 55 °C/km (Torres et al., 2004)). Since Tréhu, Flemings, et al., 2004) reported that the free gas saturation in Horizon A is high (generally greater than 50%) only above 1,060 m bsl at Site 1245 and no significant amount of free gas present in the sediments outside Horizon A, we

Table 1
Physical Model Parameters

Parameter	Value	Reference
Water depth	790 m	
Seafloor temperature	4.3 °C	Garg et al. (2008)
Initial geothermal gradient	55 °C/km	Torres et al. (2004)
Sediment grain density	2650 kg/m^3	Garg et al. (2008)
Diffusivity of methane in brine (D_m)	10^{-9} m^2/s	Garg et al. (2008)
Diffusivity of salt in brine (D_s)	10^{-9} m^2/s	Garg et al. (2008)
Solid grain radius (r_P) for sediments except Horizon A, equation (1)	1.48×10^{-6} m	Gràcia et al. (2005)
Solid grain radius (r_P) for Horizon A, equation (1)	6.80×10^{-6} m	Gràcia et al. (2005)
Pore compressibility (α_P)	10^{-8} Pa^{-1}	Rutqvist and Moridis (2009)
Thermal expansivity (α_T)	0 K^{-1}	

parameterize the sediments surrounding Horizon A that are below the inferred BGHSZ ($x < 288$ m or $x > 292$ m, and $z > 115$ m bsf) to be essentially impermeable (Figure 5). Hence, trapping of free gas is confined to the grid cells representing Horizon A. At 162.5 m bsf, the volume of the gridblocks within the gas conduit Horizon A is enlarged by about 300 times to capture the characteristic of the big volume due to the aslope extending of Horizon A mostly around the depth of 160 m bsf (Crutchley et al., 2013; Tréhu, Flemings, et al., 2004). The enlarged volume is calculated based on the length of the Horizon A between Site 1245 and Site 1250, that is, about 1.7 km (Figure 3; Tréhu, Flemings, et al., 2004).

Different physical properties are provided to the sediments vertically above and beneath the intersection of Horizon A and the BGHSZ (Tables 1 and 2), because the Horizon A aslope intersects the BGHSZ (Figure 3; Crutchley et al., 2013; Tréhu, Flemings, et al., 2004) and in the vertical direction there is a change of the sediment type across the intersection point. Vertically above the intersection point the sediments are mostly composed of hemipelagic fine-grained (clay and silty clay) sediments interbedded with turbidites (clayey silt to silty layers; Gràcia et al., 2005; Tréhu, Long, et al., 2004), while below the intersection and within the Horizon A they are predominately consisting of coarse-grained ash-rich turbidites (Tréhu, Flemings, et al., 2004; Tréhu, Long, et al., 2004).

2.5. Initial Condition

We hypothesize that the sediments within the model domain are initially not fractured and contain no faults. The initial porosity of the sediment (ϕ_0) is prescribed by an exponentially decreasing profile (Athy, 1930):

$$\phi_0 = \phi_\infty + (\phi_1 - \phi_\infty)\exp(-z/B) \tag{10}$$

where ϕ_1 is the porosity at the seafloor; ϕ_∞ is the minimum porosity at infinite depth; z is the z coordinate in the model domain, in m bsf; and B describes the exponential decay. For southern Hydrate Ridge we apply $\phi_1 = 0.63$, $\phi_\infty = 0.1$, and $B = 1{,}400$ m (Daigle & Dugan, 2010b).

The initial permeability-porosity relationship of the unfractured sediment outside Horizon A is defined by (Neuzil, 1994)

$$k_0 = \exp(C\phi_0 + D) \tag{11}$$

where k_0 is the initial permeability assigned according to ϕ_0 and C and D are the empirical coefficients. For southern Hydrate Ridge, we use $C = 13$ and $D = -40$ (Daigle & Dugan, 2010b).

For the permeable Horizon A, based on the equation of (Bryant et al., 1993)

$$k_{HA} = 0.00272 r_P^2 \tag{12}$$

a permeability of $k_{HA} = 1.26 \times 10^{-13}$ m^2 is assigned with a sediment grain radius (r_P) in Horizon A of 6.8×10^{-6} m (Gràcia et al., 2005).

Table 2
Model Equations and Parameterizations for Thermal Conductivity, Capillary Pressure, and Relative Permeability

Parameter	Value	References
Composite thermal conductivity model	$K_\Theta = (1-\phi_0)K_{dry} + \phi_0(S_a K_a + S_h K_h + S_g K_g)$	Gupta et al. (2015), Liu and Flemings (2007), and Smith, Flemings, et al. (2014)
Thermal conductivity of grains (K_{dry})[a]	3.61 W m^{-1} K^{-1}	
Capillary pressure considering the presence of hydrate phase	$P_{cap} = \sqrt{\frac{1-S_h}{k_{rS}}} P_{cap,00}$	Moridis et al. (2008)
Capillary pressure for sediments free of hydrate phase (Van Genuchten function)	$P_{cap,00} = -P_0[(S^*)^{-1/\lambda} - 1]^{1-\lambda}$ $S^* = (S_a - S_{irA})/(S_{mxA} - S_{irA})$	Moridis et al. (2008) and Van Genuchten (1980)
Van Genuchten exponent (λ)	0.45	Rutqvist and Moridis (2009)
Van-Genuchten's gas entry pressure (P_0) for matrix sediments except Horizon A	2.3×10^5 Pa	Liu and Flemings (2011)
P_0 for Horizon A	2.3×10^4 Pa	
P_0 for fractured sediments	144 Pa	Daigle et al. (2011) and Pruess and Tsang (1990)
Irreducible water saturation (S_{irA}) for unfractured sediments	0.19	
S_{irA} for fractured sediments	0.09	
Maximum water saturation (S_{mxA})	1.0	Rutqvist and Moridis (2009)
Maximum capillary pressure ($P_{cap,mx}$) for matrix sediments except Horizon A	6.5×10^7Pa	Liu and Flemings (2011)
$P_{cap,mx}$ for Horizon A	5.0×10^7Pa	
$P_{cap,mx}$ for fractured sediments	5.0×10^7Pa	
Relative permeability (modified Stone's model)	$k_{rA} = [(S_a - S_{irA})/(1 - S_{irA})]^n$ $k_{rG} = [(S_g - S_{irG})/(1 - S_{irA})]^n$	Moridis et al. (2008)
Irreducible water saturation (S_{irA}) for unfractured sediments	0.20	Rutqvist and Moridis (2009)
S_{irA} for fractured sediments	0.10	
Irreducible gas saturation (S_{irG}) for unfractured sediments	0.02	Liu and Flemings (2007) and Rutqvist and Moridis (2009)
S_{irG} for fractured sediments	0.01	
Relative permeability model (n)	3.572	Rutqvist and Moridis (2009)

[a]The thermal conductivity of sediment grains (K_{dry}) is estimated by $K_g = \prod_{j=1}^{N} K_j^{V_j} \left(\sum_{j=1}^{N} V_j = 1\right)$ (Drury & Jessop, 1983), where K_j is the thermal conductivity (Brigaud & Vasseur, 1989; Horai, 1971; Horai & Simmons, 1969) and V_j is the volume fraction (Gràcia et al., 2005) of the jth mineral.

The intrinsic permeability of the hydrate-free sediment k_i in equation (6) is thus equal to k_0 in equation (11) for the unfractured sediment except the permeable Horizon A, k_{HA} in equation (12), that is, 1.26×10^{-13} m^2 for the unfractured Horizon A; and k_{ef} in equation (5), that is, 8.3×10^{-11} m^2 for the fractured sediment after hydrofracturing.

Initially, the pore space is fully saturated with the aqueous phase containing a mass fraction of dissolved methane of 3.5×10^{-5} kg/kg at the prevailing hydrostatic pressure (Garg et al., 2008). The initial dissolved mass fraction of NaCl is 0.03185 kg/kg, corresponding to a Cl^- concentration of 558 mM (Torres et al., 2004) and a respective pore water density of 1,024 kg/m^3.

2.6. Boundary Conditions

The upper boundary at the seafloor is open with fixed temperature and pressure values applied to allow mass and heat transfer between bottom water and sediments. For the boundary condition at the seafloor, we expect that the boundary cells represent the conditions of the bottom water in connection with the sediment surface. Therefore, the boundary cells are assigned with the conditions of this bottom water, for example, the measured temperature and salinity of the bottom water as well as the pressure. The temperature and salinity of the bottom water is assumed to be constant; that is, we assume that any heat flow and salinity flux into the bottom water is effectively removed or dissipated by the bottom currents within the simulated time frame. Similarly, the lateral boundaries are chosen to be open for heat and mass transfer. In TOUGH +HYDRATE constant pressure and temperature boundary values are realized by assigning large volumes of the boundary cells (i.e., 9 orders of magnitude higher than in the inner model domain). At the bottom boundary (i.e., 500 m bsf), temperature is kept constant at 31.8 °C (calculated from the seafloor

temperature of 4.3 °C (Garg et al., 2008) and initial geothermal gradient of 55 °C/km (Torres et al., 2004)) during the model runs. Since the bottom boundary lies about 350 m below the inferred BGHSZ, latent heat associated with the hydrate reaction occurring within the GHSZ will not influence the temperature at the bottom boundary.

Methane is supplied through the bottom boundary via Horizon A, that is, the grid cells between $x = 288$ m and $x = 292$ m of the model domain. The upward methane gas supply is set to a flux of 6.5×10^{-8} kg m^{-2} s^{-1} (Garg et al., 2008), while the flux of dissolved methane (methane solubility is determined by Henry's law) is more than 1 order of magnitude lower. Hence, gaseous methane flow into the model domain dominates our simulations.

2.7. Hydraulic Parameters and Assumptions

Supplementary model parameters and equations are listed in Tables 1 and 2.

In our simulations the gas and pore water relative permeability functions are assumed to be unaltered during drainage (e.g., gas accumulation), imbibition (e.g., gas release), and secondary drainage (e.g., gas resupply). In fact, drainage, imbibition and secondary drainage curves generally differ from each other, because relative permeability functions depend not only on a given saturation but also on the direction (i.e., the given saturation is being approached from a higher or lower value) and history of the saturation change (Benson et al., 2013; Spiteri et al., 2008). This is known as the hysteresis effect, indicating the irreversibility or path dependence of multiphase flow (Benson et al., 2013; Spiteri et al., 2008). While Juanes and Bryant (2006) suggested that more attention should be paid to such hysteresis when modeling episodic events (drainage and imbibition cycles) through hydrate-bearing sediments, it is difficult to exactly constrain how hysteresis may affect our results. We expect that hysteresis in relative permeability could slightly affect the upward gas flux and the exact timing for different events, such as fracturing and gas release, but not likely change the general trend of the results.

We used a smaller irreducible water saturation (S_{irA}) for capillary pressure in compared to that for relative permeability function (Table 2). This is to avoid the unphysical situation in which the capillary pressure $P_{cap} \rightarrow -\infty$ as the water relative permeability $k_{rA} \rightarrow 0$, because in reality there are no special capillary pressure effects when liquid phase becomes immobile or discontinuous (Moridis et al., 2008). The irreducible gas or water saturation for relative permeability is set to be lower for fractured sediments compared to that for unfractured sediments (Table 2).

Most of the hydraulic parameters used in our model refer to previously published numerical simulation studies on hydrate-bearing system. A number of recent studies have investigated these parameters by experimental and/or numerical analyses, and their recommendations for parameter selection values, including those for capillary pressure or relative permeability functions, can be found in these publications (Daigle, 2016; Dai & Santamarina, 2013; Dai & Seol, 2014; Jang & Santamarina, 2014; Mahabadi et al., 2016; Mahabadi & Jang, 2014; Xu et al., 2017).

3. Results

3.1. Pressure Buildup and Initiation of Hydraulic Fracturing

Our simulations indicate that in the first 28.8-kyr gas hydrates preferentially form in the grid cells right above the BGHSZ, that is, between 110 and 125 m bsf (Figures 6b and 7b; t_1). Within this initial time gas hydrate saturations of up to 81.7% accumulate, thereby effectively reducing sediment permeability by about 9 orders of magnitude (Kossel et al., 2018). As a consequence, methane gas is trapped below this seal at the BGHSZ and pressure builds up in the grid blocks representing the gas conduit Horizon A (capillary pressure and gas relative permeability function are listed in Table 2). At time t_1, that is, after 28.8 kyr, a gas overpressure of 0.81 MPa relative to the hydrostatic pressure has been built up, exceeding the effective overburden stress, and thus, hydraulic fracturing occurs at $Z_H = 122.5$ m bsf (Figure 9a). Note that this local gas pressure increase due to buoyancy forces, makes the gas pressure to exceed the equilibrium pressure P_{eq} for hydrate formation at local temperature and salinity at greater depth, which leads to a slightly deeper BGHSZ of 125 m bsf compared to the depth of 115 m bsf observed at Hydrate Ridge during ODP Leg 204. This discrepancy is partly also a result of the vertical model grid resolution of 5 m (Figure 5). In our study we relate the model

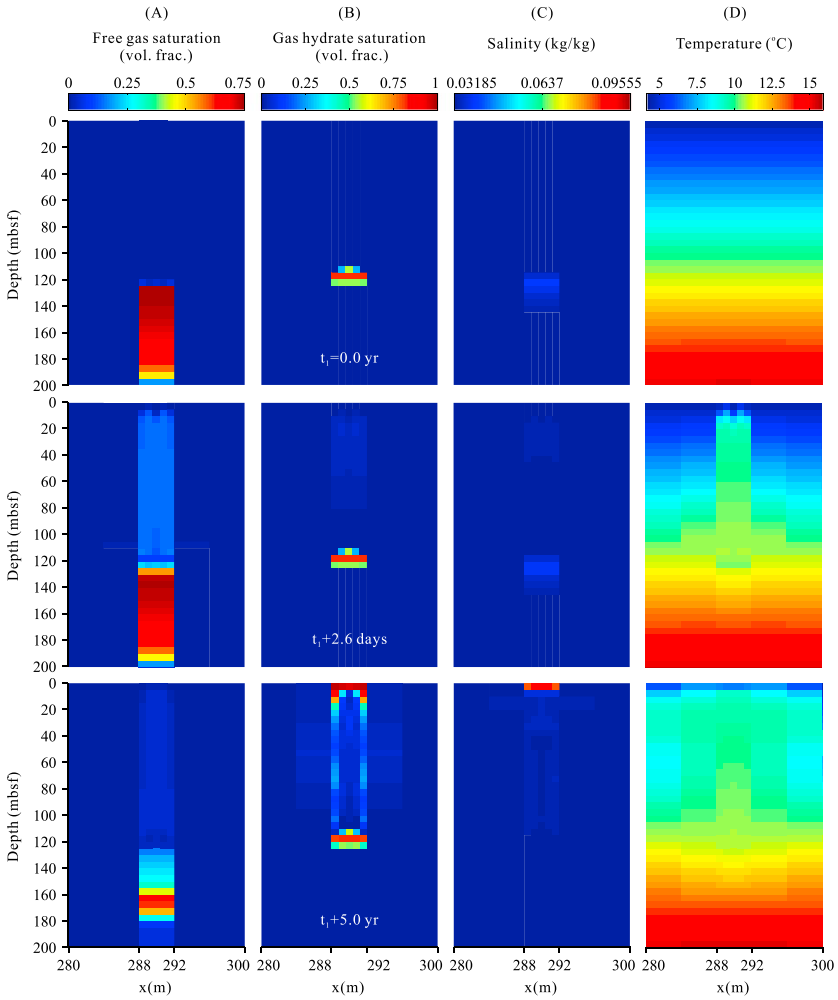

Figure 6. The 2-D simulation results around the gas conduit Horizon A in the upper 200 m of the model domain: (a) free gas saturation, (b) gas hydrate saturation, (c) salinity, and (d) temperature at different model times t_1, t_1+2.6 days, and t_1+5.0 years. $t_1 = 0$ year is the moment hydrofracturing initiated at central grid cells ($x = 288-292$ m) at 122.5 m bsf. At t_1+2.6 daysfree gas breaks through the seafloor, and at t_1+5.0 years a significant subsurface salinity peak due to gas hydrate formation has formed.

simulation time to this time of fracture initiation, that is, $t_1 = 0$ kyr (and the start of the simulation time is $t_0 = -28.8$ kyr).

The gas hydrate content is very high within the near-surface sediments (Haeckel et al., 2004; Torres et al., 2004; Tréhu et al., 2003), moderate (30–40% of pore space) in the upper tens of meters (Tréhu, Long, et al., 2004), but this is not very clear near the BGHSZ at the southern summit of Hydrate Ridge. While direct observation of hydrates in core samples is lacking, some support for our simulated concentrated hydrate layer near the BHSZ can be found at Site 1250, which was drilled ~100 m west of the southern summit of Hydrate Ridge. In Hole 1250C, mousse-like and soupy textures together with negative chloride anomalies were documented at 106–108 m bsf (i.e., just above the BSR depth of 112 m bsf), indicating dissociation of significant amounts of hydrate upon core retrieval (Tréhu et al., 2003). In Hole 1250B the log-measured electrical resistivity increase around 100 m bsf is comparable to that in the near-surface sediments (Tréhu et al., 2003), also suggesting significant amounts of hydrate near the BGHSZ.

The hydrate formation at the BGHSZ is accompanied by the release of heat and exclusion of salt. However, the rate of hydrate formation is relatively slow, and therefore, any initial temperature increase has been dissipated at t_1, that is, after 28.8 kyr (Figures 6d and 7d). Only a small peak of elevated salinity has

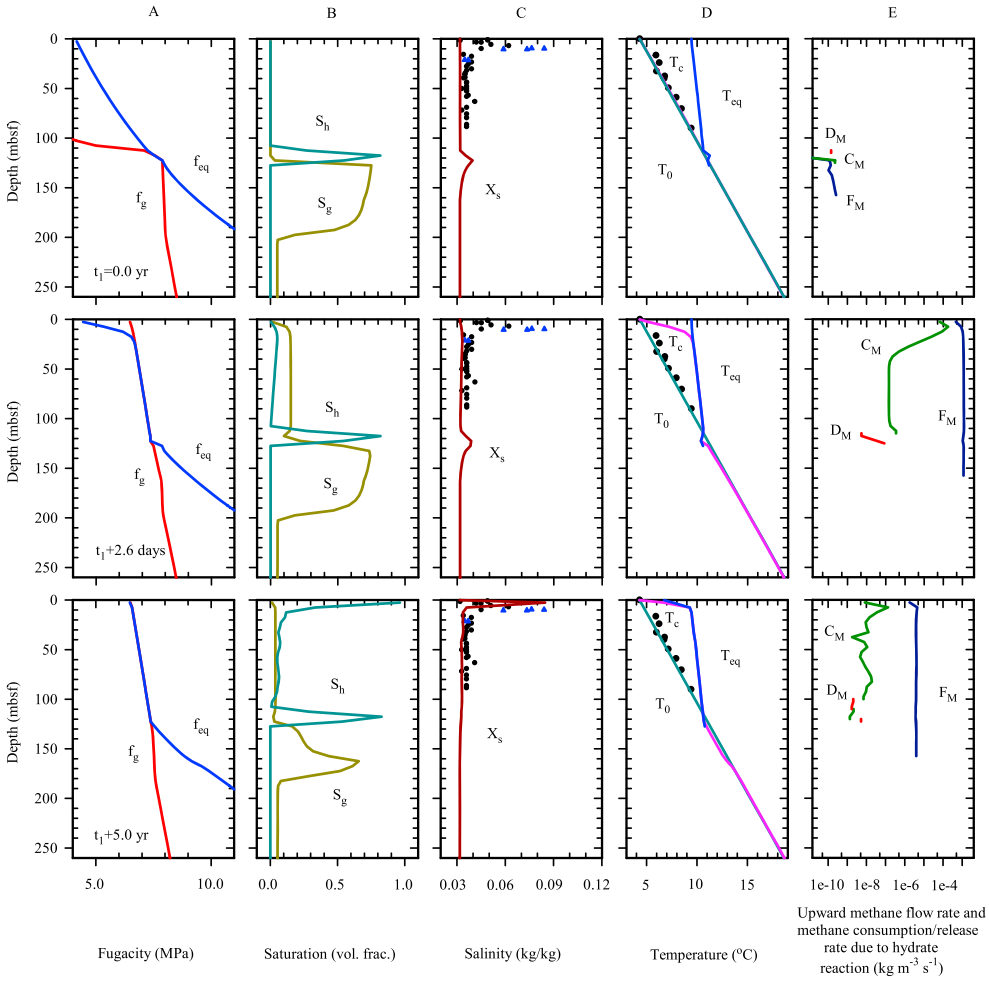

Figure 7. Model results of the central column of grid cells ($x = 289.2$ m) at different simulation times of t_1, t_1+2.6 days, and t_1+5.0 years: (a) fugacity of free methane gas (f_g) and the fugacity at three-phase equilibrium (f_{eq}); (b) free gas (S_g) and gas hydrate (S_h) saturation; (c) mass fraction of NaCl (X_s); (d) initial temperature (T_0, dark cyan), modeled temperature (T_c, pink), and three-phase equilibrium temperature (T_{eq}, blue) determined by local pressure and salinity; and (e) rates of upward methane gas flow (F_M, blue), methane consumption due to hydrate formation (C_M, green), and methane release from hydrate dissociation (D_M, red). F_M is calculated by dividing the upward gas flow rate across the bottom interface of the gridblock (kg/s) by the volume of the gridblock (m^3). Figure 7e shows the value of C_M and D_M above BGHSZ, and the value of F_M only above and near the BGHSZ, to compare C_M with F_M above the BGHSZ. For (a), Figure 8 shows an enlarged section of the f_g and f_{eq} profiles within the GHSZ indicating that $f_g > f_{eq}$, and at the same time $S_g > 0$ and $S_h > 0$ (b); hence, the system is shifted out of its strict thermodynamic equilibrium, because gas migrates through the GHSZ. In (c) black circles and blue triangles indicate the salinity measured in whole-round and dry-looking samples at ODP Site 1249, respectively (Tréhu et al., 2003). In (d) black dots indicate the measured temperature at ODP Site 1249 (Tréhu et al., 2003).

developed at t_1 (Figures 6c and 7c), because molecular diffusion is about 2 orders of magnitude smaller than heat conduction, and comparable to the rate of hydrate formation and the rate of chloride exclusion or enrichment during hydrate formation in the depth interval between 120 and 125 m bsf.

3.2. Gas Migration Through the Fractured Overburden

After the fracture network has been introduced into the overburden sediments, including the hydrate-bearing zone at 110–125 m bsf, the methane gas that has accumulated below the BGHSZ is driven rapidly toward the seafloor. In our model scenario it takes about 0.5 day for the high pore fluid pressure to propagate through the entire GHSZ, then arrive at the seafloor and finally pressurizes the entire fracture network from the BGHSZ to the seafloor. Additional 2.1 days, that is at t_1+2.6 days, are required for the gas to break

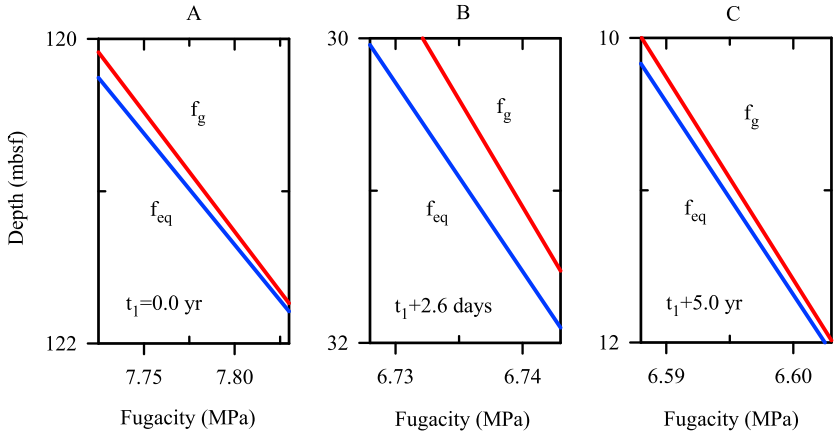

Figure 8. Zoom-in f_g and f_{eq} at certain depth for Figure 7a.

through the seafloor and establish the complete chimney structure (Figure 6a; t_1+2.6 days). The propagation of high pore fluid pressure is more rapid than the upward migration of free gas from t_1 to t_1+0.5 day. At t_1+0.5 day, the free gas front just arrives at 105 m bsf, still far away from the seafloor, while the fracturing has already reached the seafloor. Therefore, during the upward propagation of high pressure toward the seafloor, the high pressure that has induced the fracturing above 105 m bsf is exerted on the pore water.

As a consequence of fracture propagation and establishing the complete chimney structure, the gas overpressure of 0.81 MPa at the BGHSZ drops back down to the hydrostatic level (Figure 9b), and over time the remaining overpressure of 0.1–0.2 MPa in the gas accumulation below the BGHSZ will also be released (Figure 9c). After release of the overpressure, gas continues to migrate through the GHSZ due to its buoyancy, that is, the density difference between gas phase and water phase, but at a much lower rate (F_M in Figure 7e). As free gas migrates upward after fracturing has initiated at the BGHSZ, the pore water generally flows downward beneath the BGHSZ, to fill the gas conduit beneath the BGHSZ which has lost much gas within a short period of time. In this case, the pore water is not at hydrostatic condition any more. The pore water pressure is calculated to be below the local hydrostatic pressure with a significant downward pore

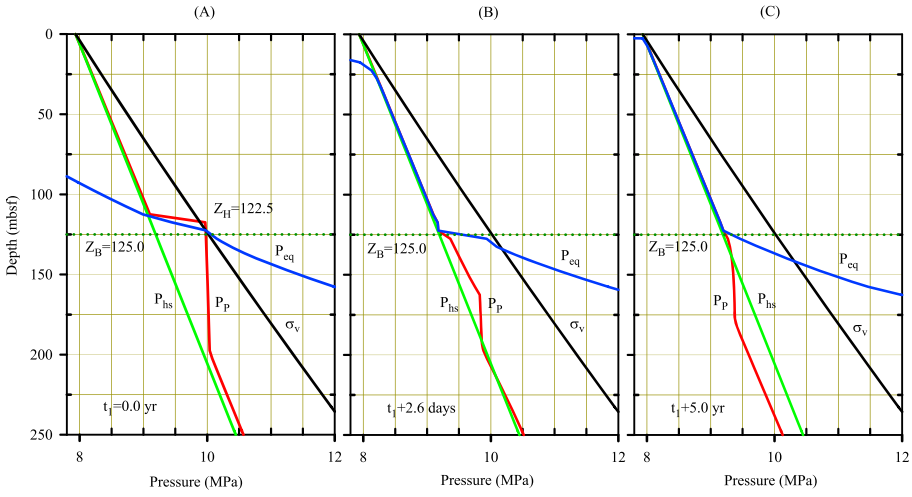

Figure 9. Modeled pressure profiles along the central cells at x = 289.2 m at different times t_1, t_1+2.6 days, and t_1+5.0 years. $Z_H$is the initiation depth of hydrofracturing, Z_B is the depth of the BGHSZ, P_{hs} is the hydrostatic pressure, P_P is the value of gas pressure when there is free gas within the intergranular space ($S_g > 0$) and is the value of pore water pressure when there is no free gas within the intergranular space ($S_g = 0$), σ_v is the overburden stress, and P_{eq} is the three-phase equilibrium pressure of methane hydrate.

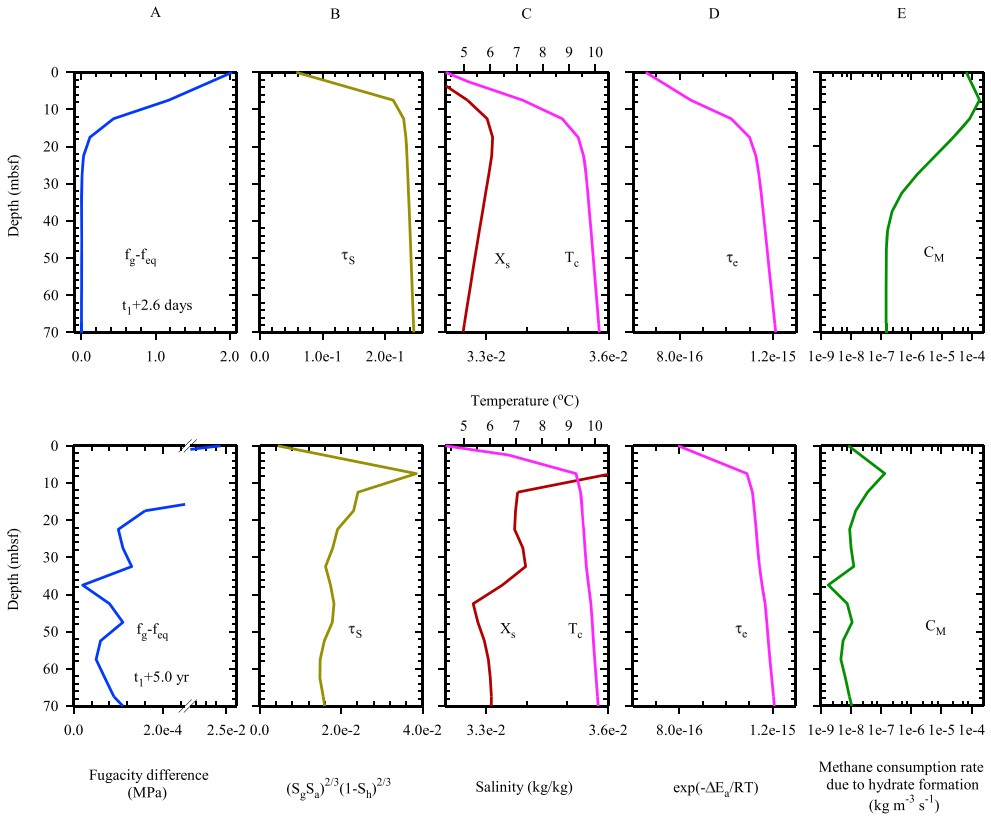

Figure 10. Zoom-in (a) fugacity difference ($f_g - f_{eq}$), (b) the value of $S_g^{2/3}S_a^{2/3}(1-S_h)^{2/3}$, (c) salinity ($X_s$) and modeled temperature (T_c), (d) the value of $\exp(-\Delta E_a/RT)$, and (e) the methane consumption rate due to hydrate formation (C_M) at t_1+2.6 days and t_1+5.0 years as shown in Figure 7. At t_1+5.0 years the fluctuations in salinity are probably because of the different hydrate formation rates and the transport by convective water flow varying both in lateral and vertical direction over time.

water flow. Therefore, the gas pressure, which is the pore pressure plus the capillary pressure, can be temporarily lower than the hydrostatic pressure (Figure 9c), but will return to hydrostatic values after a period of time and the pore water flow may also change into an upward direction.

The overpressure-driven high gas flux (F_M in Figure 7e) through the fractured sediments immediately induces hydrate formation in the GHSZ. However, the high formation rate also quickly raises the temperature in the chimney structure to about 10 °C (Figures 6d and 7d), thereby inhibiting further hydrate precipitation. As a consequence, only minor amounts of methane hydrate of a couple of percent saturation are formed within the fractured sediments (S_h in Figures 6b and 7b; t_1+2.6 days). Only in the diffusive mixing zone of bottom and pore water, that is, the uppermost 20 m bsf, hydrate formation continues at a high rate—about 3 orders of magnitude higher than in the chimney sediments below (C_M in Figure 7e; t_1+2.6 days). Hence, a subsurface salinity peak is built up while methane hydrates are filling up the available pore space in this zone. In our simulation scenario it takes about five years to reproduce a salinity peak comparable to the one observed at Hydrate Ridge ODP Site 1249 (Figure 7c; t_1+5.0 years). However, at this time elevated temperatures still prevail throughout the GHSZ, thus not matching observations at Site 1249 (Figure 7d; t_1+5.0 years).

While the elevated temperature and salinity has reduced the fugacity difference ($f_g - f_{eq}$), the driving force for hydrate formation, to a low level (Figure 10a), the hydrate formation rate can be reduced significantly (0 − 7.5 m bsf in Figure 10e) because of a low gas saturation and/or pore water saturation by decreasing the interface area (Figure 10b) participating in the hydrate formation (equation (1)). Within the near-surface sediments, the free gas saturation is low when the free gas just arrives at the seafloor (Figure 7b; t_1+2.6 days), and both, the free gas and pore water saturation, are low after the free gas venting has sustained for more

than several years because the hydrate saturation has increased to high values (Figure 7b; t_1+5.0 years). The reduction in methane consumption rate from 7.5 m bsf to the seafloor (Figure 10e) is mainly due to the low gas saturation and/or the pore water saturation (Figure 7b; t_1+2.6 days and t_1+5.0 years), which results in a low $S_g^{2/3}S_a^{2/3}(1-S_h)^{2/3}$ (Figure 10b) and thus a low interface area participating in the hydrate formation.

Beneath the near-surface sediments, at the start of free gas venting, the reduced methane consumption rate is mainly a result of the increased temperature toward greater depth (Figure 10c; t_1+2.6 days). After the free gas venting sustains for several years, the fluctuations in methane consumption rate beneath the surface sediments are mostly owing to the oscillations in the fugacity difference (Figures 10a and 10e; t_1+5.0 years). However, the fugacity difference cannot be mirrored by the change in salinity and temperature (Figures 10a and 10c; t_1+5.0 years). In this case, the fugacity difference is very low (mostly $<1.2 \times 10^{-4}$ MPa below 20 m bsf; Figure 10a; t_1+5.0 years), and the methane consumption rate is also very limited (generally $<1.0 \times 10^{-8}$ kg m^{-3} s^{-1} below 20 m bsf; Figure 10e; t_1+5.0 years). We cannot rule out some numerical instability during the calculation of gas fugacity and three-phase equilibrium fugacity when the elevated temperature and salinity has driven the system very close to three-phase equilibrium during hydrate formation. However, this numerical instability seems to be limited to the zone where the fugacity difference and the hydrate formation rate are very low, that is, not in the near-seafloor sediments. Hence, it does not affect the general trend of the hydrate formation rate, methane consumption rate, and the resulting hydrate saturation profile in the zone of interest close to the seafloor.

Close to the BGHSZ, rising temperatures due to hydrate formation in the chimney structure (Figure 7d), the existing small-salinity peak which slowly dissipates over time (Figure 7c), and the release of the overpressure (Figure 9) create highly dynamic conditions in the zone between 110 and 125 m bsf, where the existing methane hydrates are partly shifted out of their thermodynamic stability field and dissociate (D_M in Figure 7e). This, in turn, leads to some local cooling (e.g., at t_1+2.6 days the temporary decrease in temperature at about 120 m bsf is mainly due to the endothermic heat during hydrate dissociation), thereby restabilizing the hydrates again for a certain period of time. The snap shots in time depicted in Figure 7e indicate these dynamic changes between hydrate dissociation (D_M) and formation (C_M) at the BGHSZ within the simulated five years. The hydrate saturation near the BGHSZ stays almost unchanged within the five years, owing to the dynamic changes between hydrate dissociation and formation, and the low hydrate dissociation or formation rate in comparison with the rate of hydrate formation close to the seafloor.

3.3. Dissipation of Heat and Salt After Ceased Gas Venting

As methane supply from below and gas venting at the seafloor continue, the subsurface salinity spike expands to greater depth (Figure 11c), and gas hydrates form inside the GHSZ (Figure 11b). At t_1+22 years, the modeled hydrate profiles show oscillations, for example, around 50 m bsf (Figure 12a). The oscillations in hydrate saturation should be a result of the dynamic, wiggly hydrate formation rate (e.g., like the C_M in Figure 7e; t_1+5.0 years) integrating over a period of time, and thus, the oscillations are more significant after hydrate formation for several decades (e.g., Figure 12a) than hydrate formation for just several years (e.g., Figure 7b; t_1+5.0 years). At t_1+22 years hydrate saturations of up to 50% (top panel in Figure 12a) have accumulated, slightly exceeding the amount estimated from borehole data at ODP Site 1249 (Tréhu, Long, et al., 2004). Modeled temperatures are still elevated in the GHSZ, thus not matching the observed temperature profile (top panel in Figure 12c).

If the seafloor gas release and hydrate formation sustain for extended time, for example, about 60 years, the temperature can return to its initial value (Figure 11d; t_1+64 years), since the released heat is generally slightly lower than the dissipated heat when the hydrate formation rate becomes low. At this time point, high hydrate saturation and significantly increased salinity occur almost within the entire chimney structure in the GHSZ (Figures 11b and 11c; t_1+64 years). The hydrate saturation is not high outside the chimney structure (i.e., $x < 288$ m or $x > 292$ m, and $z < 80$ m bsf; Figures 11b; t_1+22 years and t_1+64 years), mainly due to the low value of $\nabla P_g - \rho_g g$ in the lateral direction, that is, low horizontal Darcy velocity of the gas phase and thus insufficient lateral gas flow from the chimney structure to the surrounding sediments. As a consequence, only low amounts of hydrate are formed outside the chimney structure and any resulting salinity elevation is effectively dissipated. Thus, outside the chimney structure the salinity stays always close to its initial value, which is equal to that of ambient seawater (Figure 11c; t_1+22 years and t_1+64 years). As

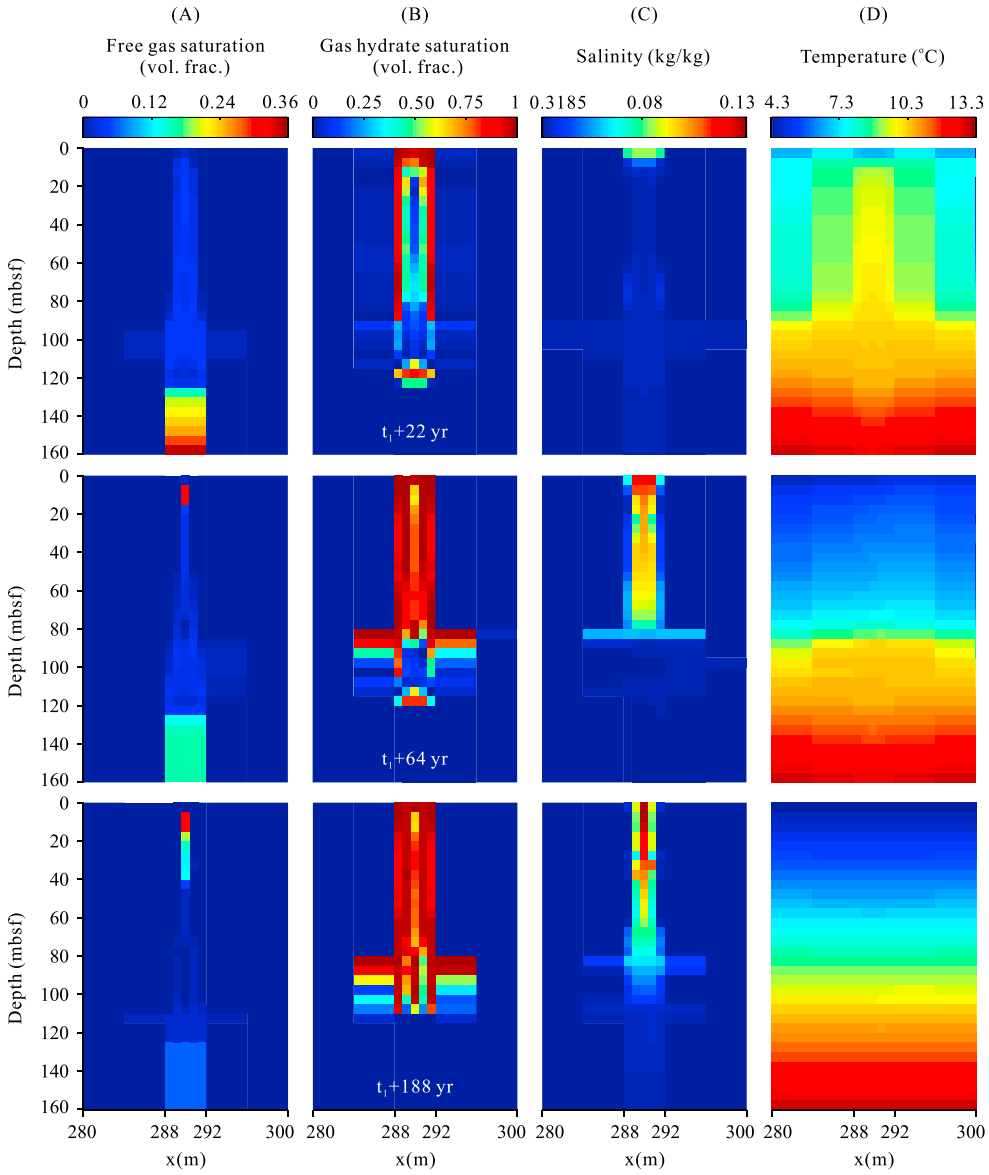

Figure 11. The 2-D simulation results around the gas conduit Horizon A in the upper 160 m of the model domain: (a) free gas saturation, (b) gas hydrate saturation, (c) salinity, and (d) temperature at different model times t_1+22, t_1+64, and t_1+188 years with a continuous gas supply and seafloor gas releasing.

the seafloor gas venting sustains over time, the free gas will disappear at the lateral boundary between the chimney structure and surrounding sediments (Figure 11a) where there are relatively lower salinity and temperature and the hydrate formation rate is relatively high. Finally, the free gas will be focused and exists only within the vertical central part of the chimney structure (x = 290 m in our model domain) where the high salinity can be limited to remove by the surrounding high-saturation hydrates (Figure 11). In response, the salinity will be significantly dissipated at the lateral boundary between the chimney structure and the surrounding sediments due to the absence of free gas and thus hydrate formation (Figure 11c; t_1+64 years and t_1+188 years).

Therefore, with a persistently continuous gas release at the seafloor and hydrate formation within the GHSZ, it is not likely to produce hydrates in high saturation near the seafloor and in low or middle saturation (e.g., 30−50%) further below, and also not the increased salinity peak exclusively near seafloor in combination with almost background temperature, as observed at Site 1249 at southern Hydrate Ridge

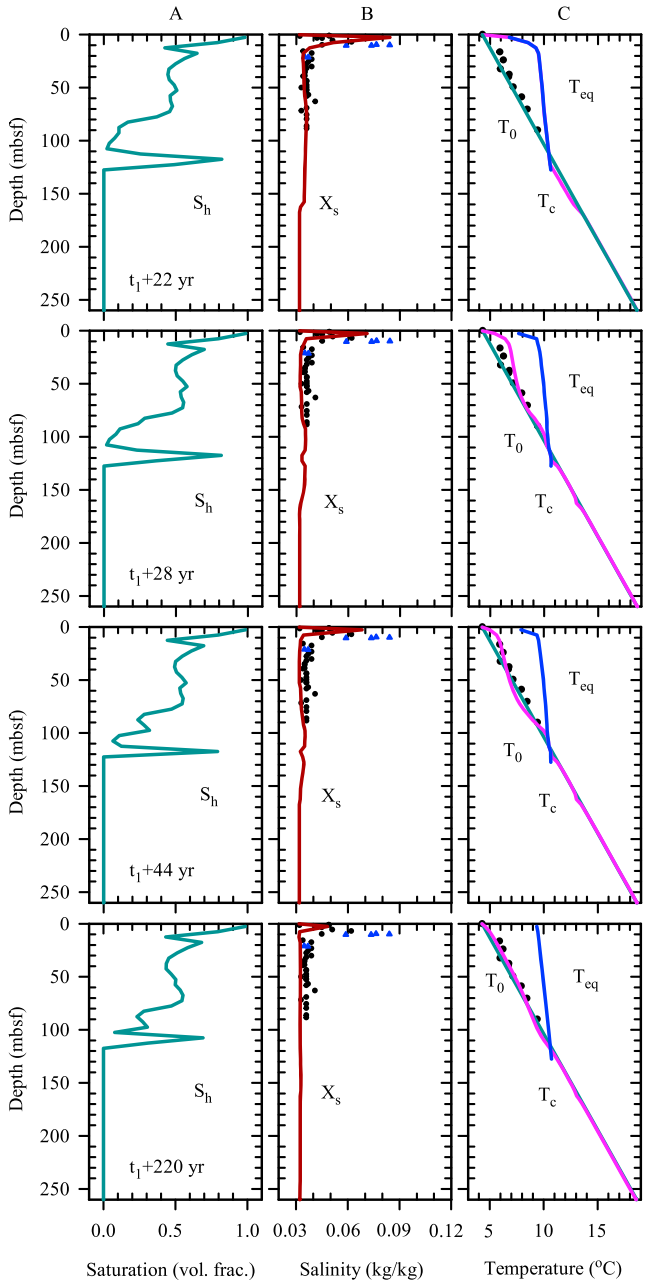

Figure 12. The evolution of (a) the gas hydrate saturation, (b) salinity, and (c) temperature along $x = 289.2$ m after stopping the gas supply from below at time t_1+22 years. In this model scenario an effective permeability of $k_{ef} = 8.3 \times 10^{-11}$ m^2 is applied for the fractured chimney sediments.

(Figures 2 and 4). Since the heat released by methane hydrate formation dissipates more rapidly than the produced salt enrichment, the increased temperature can have returned to background values while the increased salinity shrinks but still remains significant after a period of ceased hydrate formation, if hydrate formation sustains for a certain period of time, for example, about two decades (e.g., Figure 12; t_1+22 years). This suggests that hydrate formation at the southern summit of Hydrate Ridge must have ceased for some time before ODP Site 1249 was drilled, allowing to provide the observed increased salinity but a normal temperature profile. Hence, we ran additional simulations (Figure 12) in which the gas supply toward the BGHSZ was stopped after t_1+22 years by reducing the gas saturation at 162.5 m bsf (Horizon A gridblocks have a large volume due to the aslope extending of Horizon A around this depth) to be just above the irreducible gas saturation (2%). Then, some remaining gas beneath the BGHSZ can still migrate upward into the GHSZ for a short period, but several years later there is generally no free gas left within the GHSZ. Free gas saturation within the GHSZ will not remain at the irreducible gas saturation because the residual gas will be consumed by additional hydrate formation finally.

Our model simulation indicates that it takes more than 20 years for the temperature elevation to dissipate to the observed profile (panel t_1+44 years in Figure 12c) after the gas supply (and consequently gas hydrate formation) has been stopped. In Figure 12c, the heat dissipation within the GHSZ is mainly by conduction and pore water convection. The transient and variable water convection, for example influenced by spatially different permeability reductions due to nonuniform hydrate saturations, gives rise to the oscillations in temperature within the GHSZ (Figure 12c). Before the gas supply toward the BGHSZ is stopped, the decreased temperature beneath the BGHSZ (Figure 7d, t_1+5.0 years and Figure 12c, t_1+22 years) is mainly due to convective heat flow induced by downward flow of water as the free gas migrates upward into the GHSZ after fracturing. Several years later after the upward migration of free gas has ceased, the velocity of the pore water flow beneath the BGHSZ will be low in the downward direction and turns into upward direction, which leads to a rebound of the temperature beneath the BGHSZ (Figure 12c; t_1+28 years). In Figure 12c, while the temperature between 130 and 160 m bsf has mostly returned the baseline, there is still a slight reduction in temperature just near 160 m bsf (Figure 12c; t_1+28 years and t_1+44 years). This is likely related to a reduction of the gas saturation at this depth just after the gas supply has been stopped, which has slightly influenced the water flow at this depth. The gap will become narrower over time, for example, from t_1+44 years to t_1+220 years (Figure 12c).

At t_1+44 years, the modeled temperature and salinity profiles reproduce the measured data at ODP Site 1249 fairly well (Figure 12). After almost 200 years (i.e., t_1+220 years) also the salinity peak has been diminished and a linearly increasing temperature profile is established.

In Figure 12b, when the elevated temperature has almost returned to the measured values, the simulated salinity peak is comparable to the observed values in whole-round samples (black circles in Figure 12b), but slightly lower than the maximum salinity measured in dry-looking samples (blue triangles in Figure 12b) which was not disturbed by shipboard hydrate dissociation (Torres et al., 2004). To calculate a higher-salinity peak and thus match the data of dry-looking samples, we tried to enlarge the intrinsic hydrate reaction constant K_0 (even 3 orders of magnitude higher) or reduce the effective permeability

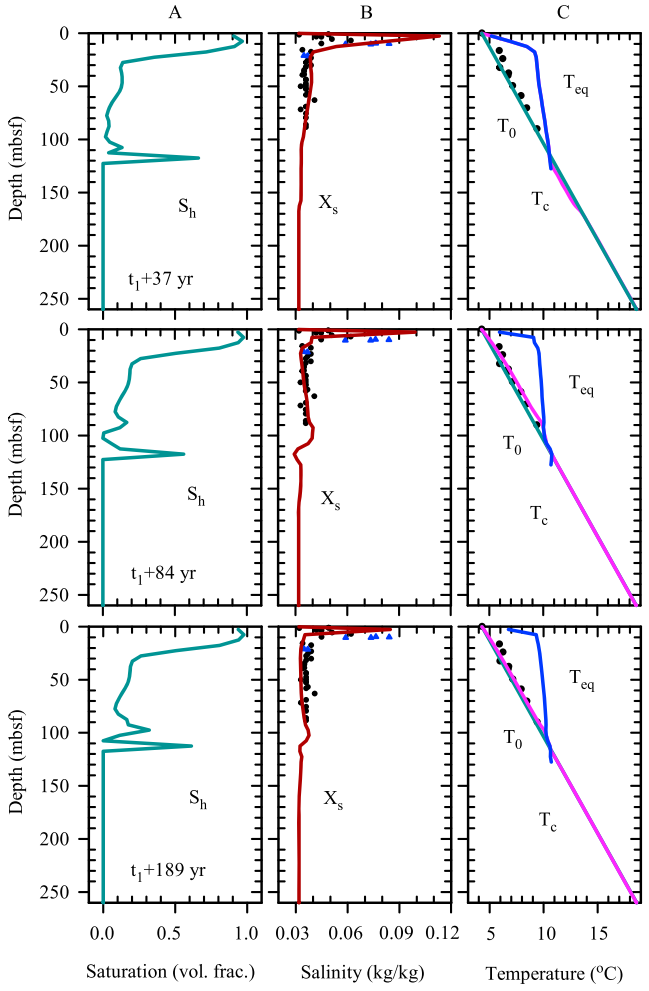

Figure 13. The evolution of (a) the gas hydrate saturation, (b) salinity, and (c) temperature along $x = 289.2$ m after stopping the free gas supply from below at time t_1+37 years. In this model scenario an effective permeability of $k_{ef} = 8.3 \times 10^{-13}$ m^2 is applied for the fractured chimney sediments.

assumed for the fractured sediments. It was speculated that, with a higher K_0, hydrate formation will be fast, and a high salinity can be developed even if the hydrate saturation is not so high and thus the water saturation is not so small, which may allow the pore water with high salinity to be more endurable for the salinity loss. However, in this case, the resulting salinity is still lower than the maximum salinity measured in dry-looking samples when the increased temperature returns around the measured values. This suggests that the process is not so sensitive to K_0.

Instead, a slightly improved fit to the observations at southern Hydrate Ridge can be achieved, by reducing the effective permeability assumed for the fractured sediments of the chimney structure serving as gas migration pathway. Keeping all other model parameters identical and reducing the intrinsic permeability by 2 orders of magnitude from $k_{ef} = 8.3 \times 10^{-11}$ m^2 to $k_{ef} = 8.3 \times 10^{-13}$ m^2 yields a higher subsurface salinity peak (panel t_1+37 years in Figure 13b). This behavior can be explained as follows: before the pore water saturation is lower than the irreducible water saturation (S_{irA}), the low intrinsic permeability helps to slow down the removal of the dissolved ions by advection, and a longer time (gas supply is stopped at t_1+37 years rather than at t_1+22 years) of simulation is conducted to build up the higher salinity. Since this salinity enrichment is initially higher than the peak measured at ODP Site 1249, after stopping the gas supply at time t_1+37 years in this model run, a considerable salinity peak remains for more than a century (panel t_1+189 years in Figure 13b). In contrast, the hydrate-induced heat pulse has dissipated completely until t_1+84 years (panel t_1+84 years in Figure 13c). Thus, our model simulation suggests that the observed subsurface salinity peak in combination with a background temperature gradient can be expected to prevail for an extended period of time, that is, several decades, at southern Hydrate Ridge. In addition, the simulation with the reduced permeability leads to the formation of lower methane hydrate saturations of only up to 30% in the chimney sediments between 30 and 100 m bsf (panel t_1+84 years in Figure 13a), which is in better agreement with average values inferred by Tréhu, Long, et al. (2004).

3.4. Initiation of a New Cycle of Gas Venting Through the GHSZ

In order to simulate the time needed to build up new overpressure that is sufficient to fracture the hydrate-clogged gas migration pathway, we again supply methane gas to the BGHSZ. Arbitrarily, we use the model result at t_1+220 years (Figure 12) as a starting point for this simulation (Figure 14). The volume enlargement at 160 m bsf due to the slope extending of Horizon A is not considered any more, partly to check a reduced time required to refracture by accumulating less free gas with a normal volume at 160 m bsf.

In the first 93 years gas is consumed by methane hydrate formation above the BGHSZ, thereby increasing the hydrate saturation at 107.5 m bsf to about 97% (Figure 14a). In return, this inhibits the gas flux across the BGHSZ (Figure 14b). At the start of the gas resupply (~0.007 year), the free gas begins to emerge and the gas saturation increases, enlarging the relative permeability of free gas, and within this short time period the hydrate saturation has not obviously increased to reduce the intrinsic permeability. Therefore, the gas flux increases at the beginning of gas resupply (Figure 14b), and then decreases due to the intrinsic permeability reduction by hydrate saturation increase and relative gas permeability reduction by the gas saturation decrease at 107.5 m bsf. As a consequence of the reduction in the gas flux across the BGHSZ, in the sediments below overpressure is slowly increasing (Figure 14c). As a result of the locally increased pressure the GHSZ is extended to larger depth, allowing further gas hydrate formation. The gaseous methane will be mostly used to form hydrate at the extended, current BGHSZ, rather than build up pressure before the elevated salinity

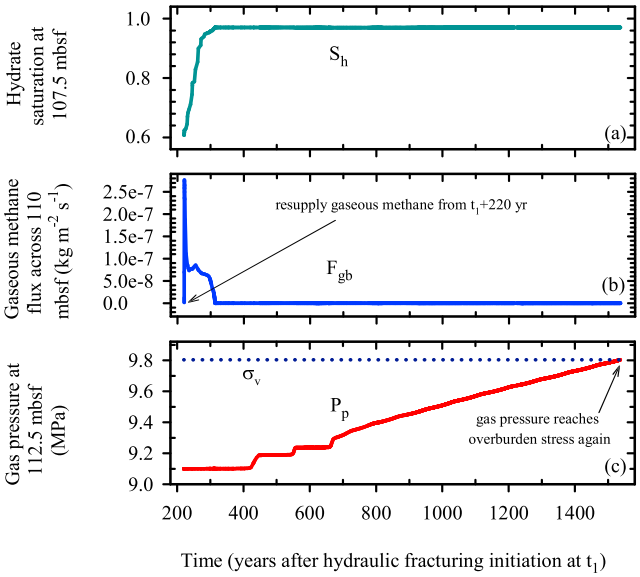

Figure 14. Restart of gas supply to the BGHSZ at the chimney structure at t_1+220 years: (a) resulting gas hydrate saturation at 107.5 m bsf, (b) methane gas flux across the base of the chimney at 110 m bsf, and (c) buildup of gas overpressure at 112.5 m bsf.

due to the additional hydrate formation has sufficiently reduced the rate of hydrate formation at the current BGHSZ. Hence, the overpressure at 112.5 m bsf is increasing stepwise before it continues to rise linearly (Figure 14c). In addition to this deepening of the BGHSZ, the stepwise increase in gas pressure for a limited period of time is also dependent on the grid discretization. With a finer grid discretization in the vertical direction, there should be more steps with a shorter time period for each step. After t_1+700 years, the equilibrium hydration pressure P_{eq} determined by the local temperature and salinity beneath the current BGHSZ has been greater than the required gas pressure to refracture, which means no more hydrate can form beneath the current BGHSZ before refracturing and allows the gas pressure to linearly rise without any more step.

Approximately at t_1+1,540 years the gas pressure would build up sufficiently to fracture the hydrate-clogged sediment at the BGHSZ again. In our model simulation, refracturing would initiate about 10 m shallower than originally (i.e., at 112.5 m bsf instead of 122.5 m bsf; see Figure 9a for comparison). This may simply be due to difference in starting conditions between this and the previous simulation.

Thus, following the refracturing of the migration pathway the release of the overpressure below the BGHSZ will drive a new cycle of gas flow, seafloor seepage, and hydrate formation until the gas flow ceases again.

4. Discussion

While the calculated timings and depths for fracture initiation, hydrate formation, and buildup of the subsurface salinity peak depend primarily on the chosen model geometry and parameterizations, such as permeability, sediment shear strength, and upward methane flux, the key effects presented above are generally applicable to methane seep systems located inside the GHSZ. In the following sections, the underlying mechanisms and implications of our simulation results will be discussed in more detail.

4.1. Heat Balance During Gas Break-Through

In order to understand the different contributions to the temperature response during the break-through of gas to the sediment surface, Figure 15 depicts the first 60 hr during which the chimney fracture network has been created. While the gas propagates through the chimney structure, the rate of gas hydrate formation is always highest at the moving gas front (Figure 15c), thereby releasing heat that raises temperature (Figures 15d and 15e).

In Figures 16e and 16m, the transferred heat H_T includes the conductive heat H_c, the convective heat due to pore water flow H_w, and the heat due to gas dissolution and gas flow H_g. The heat associated with the dissolution of gaseous methane to saturate the pore water is included in H_g. Figure 16 shows that heat transport is considerable in the chimney structure right at the time of gas break-through, which then ceases quickly (H_T in Figures 16e and 16m), while hydrate formation starts to release heat (H_R in Figures 16e and 16m). The increase in heat transport is mainly due to the increase in H_g (Figures 16e, 16g, 16m, and 16o). Figures 16d and 16l inform us that the rise of the heat due to gas dissolution and flow H_g originates from the dissolution of methane in the pore water (f_g increases in Figures 16d and 16l), which primarily happens at the ascending gas front (Figures 16a and 16i). Obviously, methane hydrates form at a very high rate during the first few hours after fracturing (Figures 16b and 16j), thus causing the temperature to increase quickly (Figures 16c and 16k). This shifts the thermodynamic equilibrium toward coexistence of free gas within less than half a day (Figures 16d and 16l; $f_g \approx f_{eq}$), and in consequence inhibits gas hydrate formation or at least drastically slows down its formation rate (Figures 16b and 16j). During the entire phase of gas break-through, heat conduction (Figures 16f and 16n) and heat transport by pore water advection (Figures 16h and 16p) do not play significant role in the heat budget.

It is the hydrate formation occurring within the first 0.5 day after the free gas front has arrived at the local depth (Figures 16b and 16j) that releases the heat and elevates the temperature to approach the

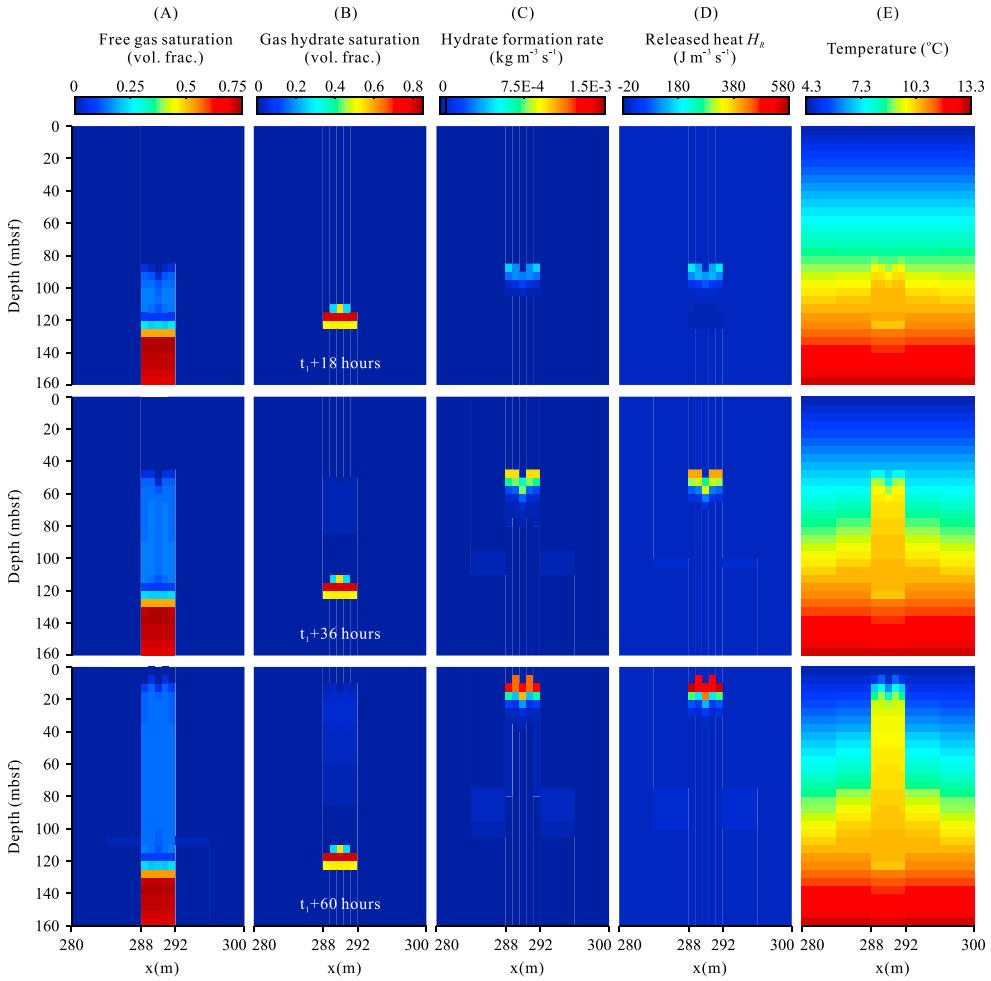

Figure 15. The 2-D simulation results around the gas migration pathway in the upper 160 m of the model domain: (a) free gas saturation, (b) methane hydrate saturation, (c) rate of methane hydrate formation, (d) rate of heat released by hydrate formation (H_R), and (e) modeled temperature (T_c) 18, 36, and 60 hr after fracturing of the overburden has occurred.

three-phase equilibrium. Within this 0.5 day the hydrate formation rate is fast (Figures 16b and 16j). For example, at 7.5 m bsf, the hydrate saturation increases to about 6% within the first 0.5 day just after the free gas occurs (Figure 16i). After the 0.5 day, the hydrate formation rate is generally slow, unless within the near-seafloor sediment where the temperatures drop toward the bottom water values. For example at t_1+5.0 years, the hydrate saturation, which is less than 10% between 20 and 100 m bsf (Figure 7b), is mostly increased during the first 0.5 day just after the free gas occurs at the local depth. The hydrate formation rate is not 2% per year on average before t_1+5.0 years; instead, the hydrate formation within the GHSZ is highly dynamic.

4.2. Methane Mass Balance

Herein, the mass balance for methane is calculated and fluxes across the seafloor are compared to observed gas venting at Hydrate Ridge.

After break-through of the gas, the methane fluxes across the seafloor (Figure 17b) stabilize at values of $1.5 - 7.5 \times 10^{-5}$ kg m^{-2} s^{-1}, until the gas accumulation below the BGHSZ has dropped to a saturation of ~10% (Figure 17a). In our simulation this takes about 80 years. Subsequently, the methane fluxes slowly decline, that is, by 1–2 orders of magnitude in ~70 years. The cumulative curves of the different contributions to the methane budget, depicted in Figure 17c, show that the largest fraction of methane is transported through the GHSZ as free gas and is emitted into the ocean. This amounts to ~77% within 150

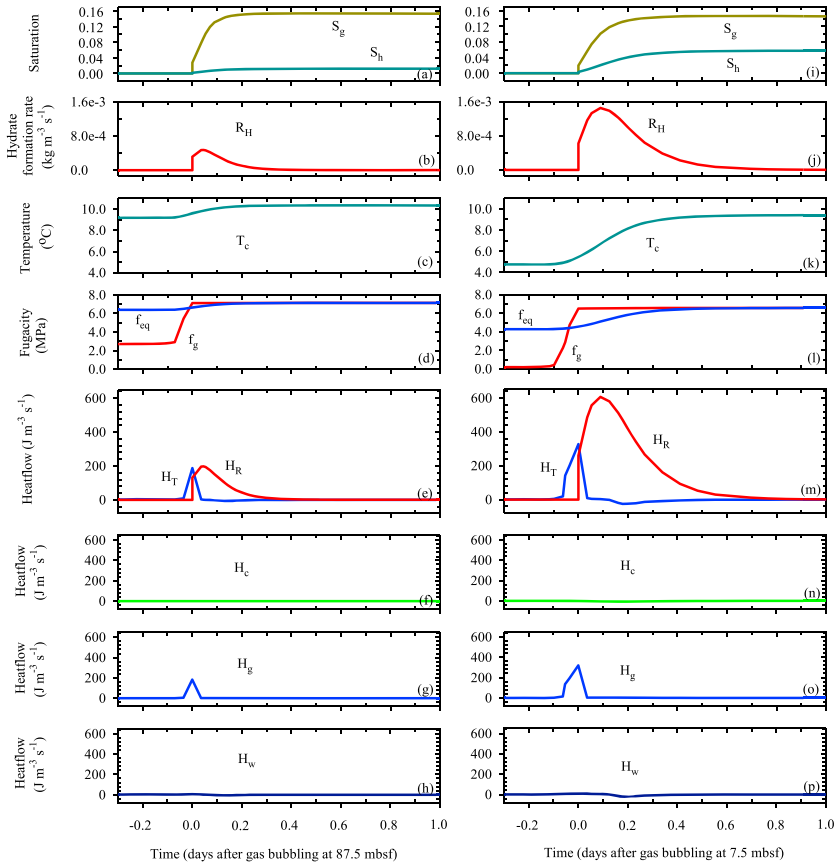

Figure 16. Evolution of process parameters and variables in the central grid point ($x = 289.2$ m) of the model domain at two arbitrary sediment depths ((left) above the BGHSZ at 87.5 m bsf and (right) 7.5 m bsf where the salinity peak forms) during the initial phase of overburden fracturing and gas break-through to the seafloor. (a and i) Methane hydrate (S_h) and gas (S_g) saturation, (b and j) rate of methane hydrate formation ($R_H > 0$) and dissociation ($R_H < 0$), (c and k) temperature (T_c), (d and l) fugacity of free methane gas (f_g) and at three-phase equilibrium (f_{eq}), (e and m) heat rate due to methane hydrate reaction (H_R: formation > 0, dissociation < 0) and transport ($H_T = H_c + H_g + H_w$), (f and n) rate of heat conduction (H_c), (g and o) rate of heat due to gas dissolution and gas flow (H_g), and (h and p) rate of heat transport by pore water advection (H_w).

years, whereas only ~20% of the methane is stored as gas hydrate and ~3% dissolves in the pore water during this time.

Heeschen et al. (2005) reported a methane gas flow of ~400 mol/hr being released over a seafloor area of 2.9×10^4 m^2 at southern Hydrate Ridge. This is equivalent to a methane seep flux of ~6×10^{-8} kg m^{-2} s^{-1}, which is 2–3 orders of magnitude lower than our simulation results (i.e., 0.25×10^{-5} kg m^{-2} s^{-1} after 150 years and up to 7.5×10^{-5} kg m^{-2} s^{-1} in the first 80 years after fracturing). Similarly, our methane flux being utilized for hydrate formation in the first 80 years of $1.5 - 7.5 \times 10^{-5}$ kg m^{-2} s^{-1} is also an order of magnitude higher than the depth-integrated rate of $0.8 - 5.5 \times 10^{-6}$ kg m^{-2} s^{-1} constrained by Haeckel et al. (2004) producing their first documentation of a near-surface chloride peak of ~809 mM at southern Hydrate Ridge.

We consider that the low Van-Genuchten's gas entry pressure of $P_0 = 144$ Pa used for the fractured chimney sediments in our simulation might be one of the reasons for these discrepancies. Our value represents a discrete fracture with an aperture of 1 mm (Daigle et al., 2011; Pruess & Tsang, 1990). In order to analyze the effect of a higher capillary pressure, we ran two additional simulations in which the Van-Genuchten's gas entry pressure P_0 was assumed to be 2.3×10^4 and 2.3×10^5 Pa for fractured sediments, respectively. The value of 2.3×10^5 Pa is equal to that used for the unfractured sediments above the BGHSZ.

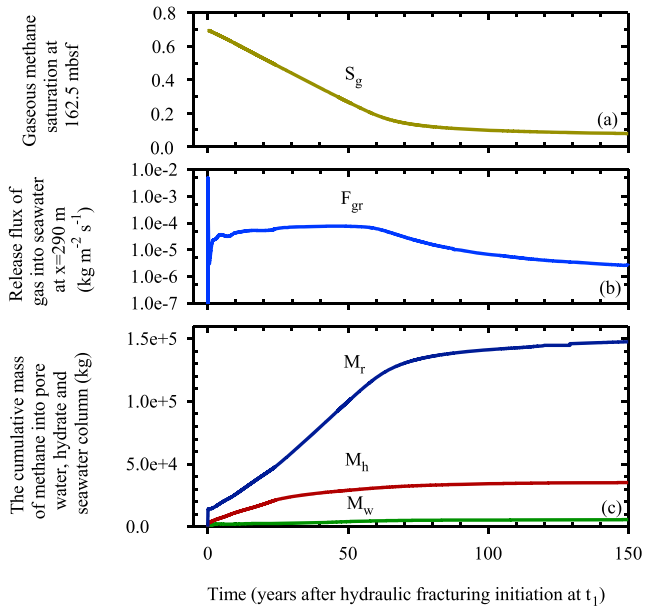

Figure 17. Evolution of (a) the gas saturation in the gas accumulation below the BGHSZ, (b) the gas flux toward the BGHSZ (arbitrarily shown is the flux $x = 290$ m bsf), and (c) the cumulative mass of methane that dissolves in the pore water (M_w), precipitates as gas hydrate (M_h), and seeps into the water column (M_r) within 150 years after fracturing of the overburden has occurred (t_1).

The simulation with $P_0 = 2.3 \times 10^4$ Pa resulted in free gas migration through the GHSZ, elevated temperature, and the occurrence of a near-surface salinity peak. These are similar to that in the simulation with $P_0 = 144$ Pa. There are also some differences between the results from these two simulations. Compared to the simulation with $P_0 = 144$ Pa, in the simulation with $P_0 = 2.3 \times 10^4$ Pa the free gas is released generally with a lower flux and for a shorter time period at the seafloor, and more hydrates occur in the lateral sediments. It means that more methane gas will be trapped within the GHSZ as hydrates instead of being emitted to overlying ocean. The reasons are as follows.

The increase in P_0 and capillary pressure will lead to a change in pore water and gas flow in the field. With a higher gas entry pressure, which means a relatively stronger effect of capillary seal, higher gas saturation is required to accumulate before the gas enters the vertically overlying gridblock, and during this time larger amount of gas can flow laterally and forms hydrate within the lateral sediment. Above the BGHSZ, after fracturing at the BGHSZ the free gas can additionally occur within the sediments 4–8 m laterally away from both boundaries of the gas chimney structure resulted in the simulation with $P_0 = 144$ Pa. However, the flux of upward free gas is generally more than 1–2 orders of magnitude lower during the upward propagation of the free gas front and during the gas release at the seafloor. This indicates that the upward free gas flow is less focused. In addition, the period of seafloor gas release can be shorter. Therefore, applying a higher gas entry pressure would reduce the resulting amount of released gas and a larger amount of methane will precipitate as hydrate, instead of being released into the ocean. This will also prolong the time for the free gas to reach the seafloor. However, the general picture of our simulations, presented here, will not change.

In the simulation with period $P_0 = 2.3 \times 10^5$ Pa the front of gaseous methane only arrives at 12.5 m bsf, which means the free gas cannot migrate through the entire GHSZ and reach the seafloor. This is because during the upward propagation of the gas front the upward gas flow is so less focused that the rate of methane supply from the less focused upward gas flow is lower than the rate of methane consumption due to hydrate formation at the shallow depth of the GHSZ. Consequently, the free gas will not occur at the shallow depth of the GHSZ, and the methane gas will not migrate through the entire GHSZ.

4.3. Persistence of the Near-Surface Salinity Peak

The hydrate saturation and the persistence of the near-surface salinity peak is strongly dependent on the hydraulic parameters (e.g., permeability, irreducible gas saturation, and irreducible water saturation) for fractured sediments of the chimney structure. The gas saturation can still be higher than the irreducible gas saturation (S_{irG}) used in the relative permeability function (assumed to be 1% for the fractured sediments in our simulations), while the water saturation is already lower than the irreducible water saturation (S_{irA}), assumed to be 10% in the relative permeability function for the fractured sediments. In this situation, gas can still enter the intergranular space and form hydrate, and then the pore water saturation decreases mainly due to an increase in hydrate saturation. After the formation of the near-surface salinity peak, the near-surface pore water saturation is generally lower than S_{irA}. After pore water saturation is lower than S_{irA}, the near-surface salinity peak is reduced solely by chemical diffusion, that is, without pore water advection. Therefore, the near-surface salinity peak can persist for several decades (e.g., Figure 12b) after seafloor gas venting and hydrate formation have stopped.

The irreducible water saturation in the relative permeability function for the fractured sediments (S_{irA}) has an influence on the duration of the near-surface salinity peak. We ran three additional simulations in which S_{irA} was assumed to be 0.002%, 2%, and 20% respectively, while all other model parameters were kept identical. The results from these three simulations are very similar to that from the simulation with $S_{irA} = 10\%$,

until salinities reach close to the salinity profile at t_1+22 years (Figure 12b). After the cessation of gas supply, in the three additional simulations the near-surface salinity peak dissipate after about 10, 30, or 300 years to decrease toward the salinity profile at t_1+220 years, whereas the salinity peak dissipated after about 198 years in the simulation with S_{irA} = 10% (Figure 12b). Therefore, our simulation results suggest that a higher S_{irA} will lead to a longer duration of the near-surface salinity peak. This can be explained by the degree at which advective chemical transport can take place in addition to chemical diffusion. Thus, depending on the assumed S_{irA} values ranging from 0.002% to 20%, the calculations show a duration of the salinity peak ranging from ten to a few hundred years.

A reduced effective permeability assumed for the fractured sediments in the chimney structure (k_{ef}) will slow down the removal of the dissolved ions by advection, before the pore water saturation is lower than S_{irA}. When a reduced k_{ef} is assumed, our simulations showed an increased total amount of dissolved ions within the fractured sediments of the chimney structure, when the pore water saturation has decreased to S_{irA}. The increased total amount of dissolved ions is more sustentative for the removal only by diffusion after the pore water saturation is lower than S_{irA}. Therefore, with a reduced k_{ef}, the salinity peak can persist longer (e.g., more than a century in Figure 13b) after the cease of seafloor gas venting and hydrate formation.

4.4. Influence of Hydrate Formation Rate

The kinetic hydrate formation rate (equation (2)) was established by laboratory experiments in the porous media composed of raw quartz sand (Li et al., 2014). Discrepancy in hydrate formation rate may exist between laboratory and natural situations. We conducted four additional simulations in which we varied the intrinsic hydrate reaction constant K_0 over 4 orders of magnitude; that is, we ran simulations with 8.06×10^2, 8.06×10^{-2}, 4.03×10^{-2}, and 2.015×10^{-2} kg m^{-2} Pa^{-1} s^{-1}, respectively, in comparison to our main simulation run with $K_0 = 8.06$ kg m^{-2} Pa^{-1} s^{-1}.

All of the additional simulations resulted in a concentrated hydrate layer at the BGHSZ where overpressure builds up and hydraulic fracturing initiates. The results from the simulations with $K_0 = 8.06 \times 10^2$, 8.06×10^{-2}, and 4.03×10^{-2} kg m^{-2} Pa^{-1} s^{-1} are similar to that using $K_0 = 8.06$ kg m^{-2} Pa^{-1} s^{-1}. After fracture initiation at BGHSZ and the start of seafloor gas release, a smaller K_0 will generally lead to a somewhat lower elevation of temperature and salinity within the same time interval (i.e., longer time required to obtain high hydrate saturation and highly elevated salinity).

In the simulation with $K_0 = 2.015 \times 10^{-2}$ kg m^{-2} Pa^{-1} s^{-1} the maximum of elevated salinity is about 0.045 kg/kg and no near-surface salinity peak occurs, even after the seafloor gas release has sustained for hundreds of years and ceased due to the exhaustion of the gas beneath the GHSZ. Given the observation of a near-surface salinity peak in the field, here we will not discuss the simulation results for a K_0 smaller than 2.015×10^{-2} kg m^{-2} Pa^{-1} s^{-1}.

It cannot make a difference to the general behavior of transient gas flow through the GHSZ as suggested from our main simulation results, even if the hydrate formation rate is significantly decreased (e.g., $K_0 = 8.06 \times 10^{-2}$ and 4.03×10^{-2} kg m^{-2} Pa^{-1} s^{-1}). This is because at these values it is also impossible to match the observed combination of "normal" temperature profile and near-surface salinity peak if there is a continuous gas flow through the GHSZ. Figure 18 shows that for these values it obviously takes longer for the induced temperature elevation to dissipate and as a consequence a broader salinity peak forms, thus not matching the observed combination of the field data. One reason for a better match in Figure 12 is that the gas supply toward BGHSZ is stopped already at t_1+22 years, but for the simulations shown in Figure 18 there is a continuous gas flow through the GHSZ and thus hydrate formation within the GHSZ, continuously releasing heat at a low rate to the surrounding, thereby slowing down the decrease of the temperature elevation. Within this longer period of time high hydrate saturations are formed throughout the GHSZ (Figures 18a and 18d), producing substantial salinity elevations at sediment depths below 20 m bsf (Figures 18b and 18e).

4.5. Focused and Intermittent Methane Gas Flow Through the GHSZ

Essentially, methane gas can effectively migrate through the GHSZ if the gas flow rate exceeds the rate of methane consumption into gas hydrates (e.g., Figure 7e). Our simulations demonstrate that this condition is satisfied if the gas supply to the BGHSZ is sufficiently high to create an overpressure that fractures the

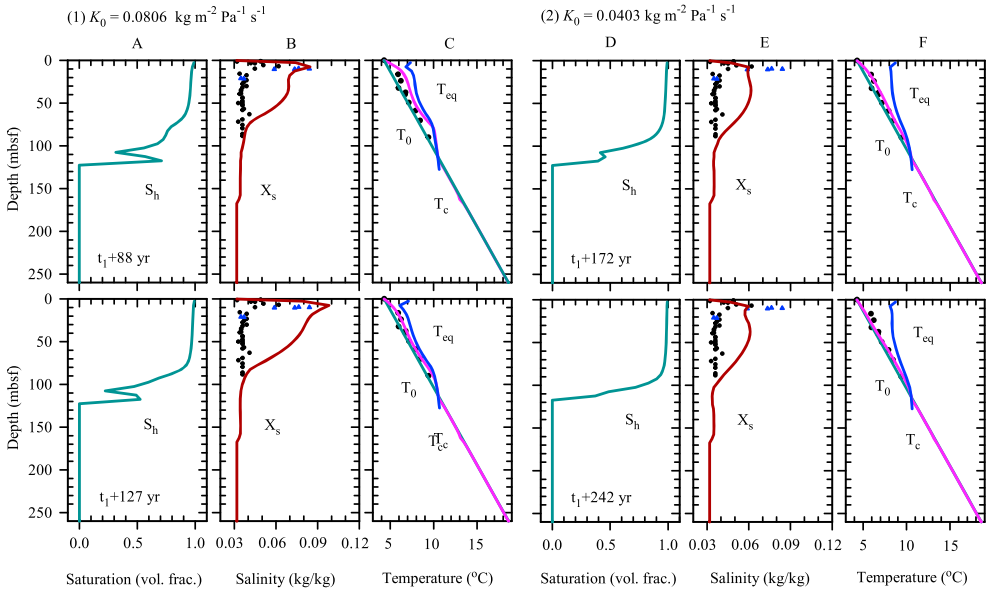

Figure 18. The evolution of (a and d) the gas hydrate saturation, (b and e) salinity, and (c and f) temperature along $x = 289.2$ m when the intrinsic hydrate reaction constant K_0 is assumed to be 8.06×10^{-2} and 4.03×10^{-2} kg m^{-2} Pa^{-1} s^{-1}, respectively.

overburden sediments. In these highly permeable migration pathways, gas can break through the GHSZ and reach the seafloor. At this stage, the gas flow has shifted the system out of the strict thermodynamic equilibrium. In addition, latent heat released by the induced formation of methane hydrates raises the temperature toward the three-phase equilibrium boundary, thereby further reducing the methane hydrate reaction rate and thus, further facilitating the gas transport. Such focused migration pathways are common seep features that fuel cold vents with methane gas from below, also in water depths where gas hydrates can form (e.g., Berndt, 2005; Crutchley et al., 2010; Riedel et al., 2002).

However, elevated temperatures and salinities in the GHSZ that are characteristic of active gas hydrate formation have rarely been reported (Haeckel et al., 2004; Koch et al., 2016; Römer et al., 2012; Torres et al., 2004). In most instances these anomalies are related to mud volcanoes and seeps connected to salt diapirs, where temperature and salinity signals from sediment depths of several kilometers are advected toward the seafloor (e.g., Aloisi et al., 2004; Haffert et al., 2013; Hensen et al., 2007, 2004; Reitz et al., 2007; Reitz et al., 2011). Here we can exclude any influence from such deep processes based on the geochemical data (e.g., Figure 1) and seismic information. Our simulations indicate that sufficiently high fluxes of methane gas in the GHSZ on the order of $10^{-5} - 10^{-3}$ kg m^{-2} s^{-1} are required to generate a near-surface salinity peak as observed at southern Hydrate Ridge (Figure 7). In addition, the model runs suggest that the supplied methane gas at high-flux and salinity peak can only exist temporarily, because continuing gas supply will broaden the salinity enrichment downward as gas hydrate saturations further increase in the entire GHSZ, thereby slowly clogging up the gas migration pathway (Figure 11b). In addition, broad salinity enrichments spanning the entire GHSZ also result from much lower, but continuous methane supply rates as applied in the 1-D simulations of Liu and Flemings (2007) and Garg et al. (2008).

The intermittency of the gas flow through the GHSZ is also evident from the observed combination of salinity peak and background heat flow at southern Hydrate Ridge (Figures 2 and 4). Our simulations suggest that this is only possible after gas migration through the chimney structure has ceased. Likely reasons are reduced permeability from fracture- and pore-filling gas hydrates in the migration pathway and decayed overpressure in the gas accumulation below the BGHSZ. After the gas flux into the GHSZ has stopped (or decreased sufficiently) gas hydrate formation will also end. Subsequently, the temperature elevation will dissipate more quickly than the salinity peak, because heat conduction is at least 2 orders of magnitude faster than molecular diffusion. As a result, a linearly increasing thermal gradient in the chimney structure will develop within a few decades, whereas the subsurface salinity peak can prevail for several decades (Figure 12b) or a couple of hundreds of years (Figure 13b).

4.6. General Implications for Methane Gas Migration Through the GHSZ

Matsumoto, Kakuwa, et al. (2017) and Matsumoto, Tanahashi, et al. (2017) presented drill core and logging results of several hydrate-choked chimney structures in the Sea of Japan that exhibit massive, several meters thick gas hydrate layers right below the seafloor and continuous gas hydrate saturations of 80–100% in the entire structure down to the BGHSZ. While our model parameters were different from the parameters at the Sea of Japan sites, our modeled gas hydrate saturations after a continuous gas supply for about 60 or 180 years (Figure 11b) agree with their observations at the Sea of Japan sites. This may underline that our simulation results can be generalized for cold vents/gas chimney settings. Unfortunately, Matsumoto, Kakuwa, et al. (2017) and Matsumoto, Tanahashi, et al. (2017) did not show any salinity or temperature profiles for their sites, and they just reported high thermal gradients (but it is unclear if this is the background value or measured value in the chimney).

The modeled trends from our simulations and the described dynamic process of methane gas migration through the GHSZ are representative of the general mechanisms occurring at cold vents that are typically underlain by gas chimney structures. Our simulations also explain, under which conditions massive subseafloor hydrates and chloride anomalies can be observed and why both features are exclusively found in near-seafloor sediments. The key driver or condition that enables methane gas to migrate through the GHSZ is the focused, high-flux methane gas supply through the BGHSZ. For example, at southern Hydrate Ridge the initially required high flux of methane gas through the BGHSZ is on the order of 10^{-5} kg m^{-2} s^{-1} which can be achieved by hydraulic fracturing near the BGHSZ due to a period of upward free gas migration at relatively low flux from larger depth that builds up overpressure below the BGHSZ (the simulated case in our work) or by the direct supply at high flux from depth. With this magnitude of flux supplied directly through the BGHSZ, the methane gas can migrate through the GHSZ even if there is no highly permeable pathway previously existing from the BGHSZ to the seafloor, because those paths will be created by fracturing when the free gas arrives at the shallow depth of the GHSZ where the sediments have a low effective stress and then builds up overpressure. This has been confirmed by our additional simulations for a generalized geological case, during which we assumed that the Horizon A beneath the BGHSZ is not confined and thus the lateral gas migration across the boundary between Horizon A and surrounding sediment is allowed. The focused, high-flux methane gas supply through the BGHSZ allows the methane gas transport through the GHSZ, because during the upward free gas migration the rate of upward methane gas flow will be sufficiently high to exceed the methane consumption rate by hydrate formation within the GHSZ.

Confined by the salinity and temperature observed in the field, we further restrict that the supplied methane gas through the BGHSZ is not only focused, at high flux, but also intermittent. With this focused and intermittent methane gas supply through the BGHSZ our simulations provide explanations why only few observational data for salinity and temperature elevations with relation to gas hydrate formation exist, despite the fact that gas seeps in the gas hydrate stability zone are found ubiquitously at the worldwide margins (although numbers are drastically reduced compared to seeps in shallower water depths outside the GHSZ (e.g., Naudts et al., 2006)). Thus, coring for the chimney structures in the global marine gas hydrate provinces has to target the right spot at the right time to observe gas venting, salinity, and temperature elevations.

5. Conclusions

We have conducted two-dimensional numerical simulations of focused gas flow through the GHSZ that is being observed at many cold seeps worldwide. The well-studied southern summit of Hydrate Ridge served as a case study site, and we successfully constrained the conditions under which the salinity, temperature, and gas hydrate data of ODP Site 1249 can be reproduced. Our simulations suggest that gas migration through the GHSZ is, fundamentally, a result of methane gas supply in excess of its consumption by hydrate formation. The required high gas flux is driven by local overpressure, built up from gas accumulating below the base of the GHSZ that fractures the overburden when exceeding a critical pressure, thereby creating a chimney-like migration pathway. Initially rapid hydrate formation raises the temperature in the chimney structure, thereby further facilitating the gas transport through the GHSZ. As a consequence, high hydrate saturations form preferentially close to the seafloor, where temperatures drop to bottom water values, producing a prominent subsurface salinity peak. Subsequently, gas hydrates form at a much lower rate

throughout the chimney structure, further reducing its permeability until the methane supply from below ceases. The initial temperature elevation and salinity enrichment will then slowly dissipate, while overpressure builds up again below the BGHSZ until a new cycle of gas break-through can start. Thus, our simulations suggest that the near-surface salinity peak and elevated temperatures are the result of transient high-flux gas migration through the GHSZ.

Notations

A	Surface area involved in the hydrate reaction (m^2), equation (1)
B	Constant for describing the exponential decay of the porosity against depth, equation (10)
C, D	Empirical coefficients used in the intrinsic permeability-porosity relationship of the unfractured sediment outside Horizon A, equation (11)
C_M	Methane consumption rate due to hydrate formation (kg m^{-3} s^{-1})
d	Fracture aperture (m), equations (4), (5), (8), and (9)
d_h	Changed fracture aperture due to hydrate precipitation (m), equations (8) and (9)
D_M	Methane release rate due to hydrate dissociation (kg m^{-3} s^{-1})
f_{eq}, f_g, f_d	Gas fugacity at thermodynamic equilibrium, actual gas fugacity, and fugacity of dissolved methane (Pa), equation (2)
F_{gb}	Gaseous methane flux across 110 m bsf during pressure buildup to refracture (kg m^{-2} s^{-1}), Figure 14b
F_{gr}	Release flux of gas into seawater at x = 290 m (kg m^{-2} s^{-1}), Figure 17b
g	Acceleration due to gravity (m/s^2)
H_c, H_g, H_w	Rate of heat conduction, rate of heat transport by gas migration, and rate of heat transport by pore water advection (J m^{-3} s^{-1})
H_R	Rate of heat released by hydrate formation (J m^{-3} s^{-1})
H_T	Rate of conductive and advective heat transport ($H_T = H_c+H_g+H_w$; J m^{-3} s^{-1})
K_0	Intrinsic hydrate reaction constant for hydrate formation and dissociation (kg m^{-2} Pa^{-1} s^{-1}), equation (2)
k	Intrinsic permeability of sediment considering the presence of hydrate in the intergranular space (m^2), equation (6)
k_0, k_{HA}, k_{ef}	Intrinsic permeability for unfractured sediment except the permeable Horizon A, intrinsic permeability for sediment within unfractured Horizon A, and equivalent permeability for the fracture network within the gas chimney structure when the sediment does not contain hydrate (m^2), equations (11), (12), and (5)
$k_{ef\text{-}h}$	Equivalent permeability for the fracture network within the gas chimney structure while considering the presence of hydrate (m^2), equation (9)
k_{fracture}	Permeability of each discrete fracture (m^2), equation (4)
k_i	Intrinsic permeability of the sediment free of hydrate (=k_0,k_{HA},or k_{ef}; m^2), equation (6)
k_{rS}	Permeability adjustment factor due to the presence of hydrate, equations (6) and (7)
l	The interfracture spacing (m), equations (5) and (9)
M_{CH_4}, M_{Hyd}	Molecular weight of CH_4, and molecular weight of hydrate (kg/mol), equation (2)
M_h, M_r, M_w	Cumulative mass of methane that precipitates as hydrate, releases into the water column, and dissolves in the pore water (kg), Figure 17c
n_H	Permeability reduction exponent due to hydrate formation, equation (7)
N_V	Number of interstitial pore spaces in a unit volume of bulk sediment, equation (1)
P_{eq}	Three-phase equilibrium pressure for hydrate reaction (Pa), Figure 9
P_{hs}	Hydrostatic pressure (Pa), Figure 9
P_P, P_g	Pore pressure and gas pressure (Pa)
P_w	Pore water pressure (Pa)
R	Universal gas constant (J mol^{-3} K^{-1}), equation (2)
R_H	Rate of hydrate reaction (kg m^{-3} s^{-1})
R_M	The methane consumption or release rate due to hydrate reaction (kg m^{-3} s^{-1}), equation (2)
r_P	Solid grain radius (m), equations (1) and (12)
S_a, S_g, S_h	Volumetric saturations of aqueous pore water, free gas, and hydrate

T	Absolute temperature (=T_c+273.15) in K, equations (2) and (3)
T_0, T_c, T_{eq}	Initial temperature determined by the initial geothermal gradient, current or modeled temperature, and three-phase equilibrium temperature determined by local pressure and salinity (°C)
V_V	The volume of each interstitial pore space (m^3)
x	x coordinate in the model domain (m), Figure 5
X_s	Mass fraction of NaCl (kg/kg)
z	z coordinate in the model domain (m bsf), Figure 5
Z_B	Depth of the BGHSZ (m bsf), Figure 9
Z_H	Initiation depth of hydrofracturing (m bsf), Figure 9
ΔE_a	Hydrate activation energy (J/mol), equation (2)
ΔH	Hydrate reaction enthalpy (kJ/kg), equation (3)
ρ_g	Density of gaseous methane (kg/m^3)
σ_v	Local overburden stress (Pa), Figure 9
τ_e	The term of $\exp(-\Delta E_a/RT)$ during calculating R_M, equation (2) and Figure 10d
τ_S	The term of $S_g^{2/3}S_a^{2/3}(1-S_h)^{2/3}$ during calculating A, equation (1) and Figure 10b
ϕ_0	Porosity, equations (10) and (11)
ϕ_1, ϕ_∞	Porosity at the seafloor, and minimum porosity at infinite depth, equation (10)
ϕ_c	Critical porosity, equation (7)

Acknowledgments
All the data used are listed in the references or archived in the Figshare repository (https://figshare.com/articles/JGR-Solid_Earth_manuscript_2019JB017417_data_zip/7925306). This work was supported by the National Natural Science Foundation of China (41176052, 41576035, 41276050), the Natural Science Foundation of Guangdong Province (S2013010014523), the Innovation Development Fund of South China Sea Eco-Environmental Engineering Innovation Institute of the Chinese Academy of Sciences (ISEE2018PY02), and UCAS Joint PhD Training Program (UCAS[2015]37). Additional funding was provided through the HGF-CAS Joint Research Group (project 208) and the German SUGAR project (BMBF grant 03G0856A). Lawrence Berkeley National Laboratory received support by the U.S. Department of Energy under contract DE-AC02-05CH11231. The authors gratefully acknowledge Douglas Schmitt, Brandon Dugan, André Revil, Sheng Dai, Hugh Daigle, Xiaoli Liu, an anonymous Associate Editor, and five anonymous reviewers for their constructive comments on the manuscript.

References

Aloisi, G., Drews, M., Wallmann, K., & Bohrmann, G. (2004). Fluid expulsion from the Dvurechenskii mud volcano (Black Sea): Part I. Fluid sources and relevance to Li, B, Sr, I and dissolved inorganic nitrogen cycles. *Earth and Planetary Science Letters*, *225*(3-4), 347–363. https://doi.org/10.1016/j.epsl.2004.07.006

Athy, L. F. (1930). Density, porosity, and compaction of sedimentary rocks. *AAPG Bulletin*, *14*(1), 1–24.

Behrmann, J. H. (1991). Conditions for hydrofracture and the fluid permeability of accretionary wedges. *Earth and Planetary Science Letters*, *107*(3-4), 550–558. https://doi.org/10.1016/0012-821X(91)90100-V

Benson, S., Pini, R., Reynolds, C., & Krevor, S. (2013). Relative permeability analyses to describe multi-phase flow in CO2 storage reservoirs (Technical report). Melbourne, VIC, Australia: Global CCS Institute.

Berndt, C. (2005). Focused fluid flow in passive continental margins. *Philosophical Transactions of the Royal Society A: Mathematical, Physical and Engineering Sciences*, *363*(1837), 2855–2871. https://doi.org/10.1098/rsta.2005.1666

Brigaud, F., & Vasseur, G. (1989). Mineralogy, porosity and fluid control on thermal conductivity of sedimentary rocks. *Geophysical Journal International*, *98*(3), 525–542. https://doi.org/10.1111/j.1365-246X.1989.tb02287.x

Bryant, S. L., King, P. R., & Mellor, D. W. (1993). Network model evaluation of permeability and spatial correlation in a real random sphere packing. *Transport in Porous Media*, *11*(1), 53–70. https://doi.org/10.1007/BF00614635

Bünz, S., Polyanov, S., Vadakkepuliyambatta, S., Consolaro, C., & Mienert, J. (2012). Active gas venting through hydrate-bearing sediments on the Vestnesa Ridge, offshore W-Svalbard. *Marine Geology*, *332-334*, 189–197. https://doi.org/10.1016/j.margeo.2012.09.012

Castellini, D. G., Dickens, G. R., Snyder, G. T., & Ruppel, C. D. (2006). Barium cycling in shallow sediment above active mud volcanoes in the Gulf of Mexico. *Chemical Geology*, *226*(1-2), 1–30. https://doi.org/10.1016/j.chemgeo.2005.08.008

Clennell, M. B., Hovland, M., Booth, J. S., Henry, P., & Winters, W. J. (1999). Formation of natural gas hydrates in marine sediments: 1. Conceptual model of gas hydrate growth conditioned by host sediment properties. *Journal of Geophysical Research*, *104*(B10), 22,985–23,003. https://doi.org/10.1029/1999JB900175

Crutchley, G. J., Berndt, C., Geiger, S., Klaeschen, D., Papenberg, C., Klaucke, I., et al. (2013). Drivers of focused fluid flow and methane seepage at south Hydrate Ridge, offshore Oregon, USA. *Geology*, *41*(5), 551–554. https://doi.org/10.1130/G34057.1

Crutchley, G. J., Pecher, I. A., Gorman, A. R., Henrys, S. A., & Greinert, J. (2010). Seismic imaging of gas conduits beneath seafloor seep sites in a shallow marine gas hydrate province, Hikurangi Margin, New Zealand. *Marine Geology*, *272*(1-4), 114–126. https://doi.org/10.1016/j.margeo.2009.03.007

Dai, S., & Santamarina, J. C. (2013). Water retention curve for hydrate-bearing sediments. *Geophysical Research Letters*, *40*, 5637–5641. https://doi.org/10.1002/2013GL057884

Dai, S., & Seol, Y. (2014). Water permeability in hydrate-bearing sediments: A pore-scale study. *Geophysical Research Letters*, *41*, 4176–4184. https://doi.org/10.1002/2014GL060535

Daigle, H. (2016). Relative permeability to water or gas in the presence of hydrates in porous media from critical path analysis. *Journal of Petroleum Science and Engineering*, *146*, 526–535. https://doi.org/10.1016/j.petrol.2016.07.011

Daigle, H., Bangs, N. L., & Dugan, B. (2011). Transient hydraulic fracturing and gas release in methane hydrate settings: A case study from southern Hydrate Ridge. *Geochemistry, Geophysics, Geosystems*, *12*, Q12022. https://doi.org/10.1029/2011GC003841

Daigle, H., & Dugan, B. (2010a). Effects of multiphase methane supply on hydrate accumulation and fracture generation. *Geophysical Research Letters*, *37*, L20301. https://doi.org/10.1029/2010GL044970

Daigle, H., & Dugan, B. (2010b). Origin and evolution of fracture-hosted methane hydrate deposits. *Journal of Geophysical Research*, *115*, B11103. https://doi.org/10.1029/2010JB007492

Daigle, H., & Dugan, B. (2011). Capillary controls on methane hydrate distribution and fracturing in advective systems. *Geochemistry, Geophysics, Geosystems*, *12*, Q01003. https://doi.org/10.1029/2010GC003392

Dickens, G. R. (2003). Rethinking the global carbon cycle with a large, dynamic and microbially mediated gas hydrate capacitor. *Earth and Planetary Science Letters*, *213*(3-4), 169–183. https://doi.org/10.1016/S0012-821X(03)00325-X

Drury, M. J., & Jessop, A. M. (1983). The estimation of rock thermal conductivity from mineral content: an assessment of techniques. *Zentralblatt für Geologie und Paläontologie*, *1*, 35–48.

Garg, S. K., Pritchett, J. W., Katoh, A., Baba, K., & Fujii, T. (2008). A mathematical model for the formation and dissociation of methane hydrates in the marine environment. *Journal of Geophysical Research*, *113*, B01201. https://doi.org/10.1029/2006JB004768

Ginsburg, G., & Soloviev, V. (1997). Methane migration within the submarine gas-hydrate stability zone under deep-water conditions. *Marine Geology*, *137*(1-2), 49–57. https://doi.org/10.1016/S0025-3227(96)00078-3

Gràcia, E., Martínez-Ruiz, F., Piñero, E., Cruz Larrasoaña, J., Vizcaino, A., & Ercilla, G. (2005). Data report: Grain-size and bulk and clay mineralogy of sediments from the summit and flanks of southern Hydrate Ridge, Sites 1244–1250, ODP Leg 204. In A. M. Tréhu, G. Bohrmann, M. E. Torres, & F. S. Colwell (Eds.), *Proc. ODP, Sci. Results* (Vol. 199, pp. 1–19). College Station, TX: Ocean Drilling Program. https://doi.org/10.2973/odp.proc.sr.204.110.2006

Gupta, S., Helmig, R., & Wohlmuth, B. (2015). Non-isothermal, multi-phase, multi-component flows through deformable methane hydrate reservoirs. *Computational Geosciences*, *19*(5), 1063–1088. https://doi.org/10.1007/s10596-015-9520-9

Haeckel, M., Suess, E., Wallmann, K., & Rickert, D. (2004). Rising methane gas bubbles form massive hydrate layers at the seafloor. *Geochimica et Cosmochimica Acta*, *68*(21), 4335–4345. https://doi.org/10.1016/j.gca.2004.01.018

Haffert, L., Haeckel, M., Liebetrau, V., Berndt, C., Hensen, C., Nuzzo, M., et al. (2013). Fluid evolution and authigenic mineral paragenesis related to salt diapirism—The Mercator mud volcano in the Gulf of Cadiz. *Geochimica et Cosmochimica Acta*, *106*, 261–286. https://doi.org/10.1016/j.gca.2012.12.016

Heeschen, K. U., Collier, R. W., de Angelis, M. A., Suess, E., Rehder, G., Linke, P., & Klinkhammer, G. P. (2005). Methane sources, distributions, and fluxes from cold vent sites at Hydrate Ridge, Cascadia Margin. *Global Biogeochemical Cycles*, *19*, GB2016. https://doi.org/10.1029/2004GB002266

Heeschen, K. U., Tréhu, A. M., Collier, R. W., Suess, E., & Rehder, G. (2003). Distribution and height of methane bubble plumes on the Cascadia Margin characterized by acoustic imaging. *Geophysical Research Letters*, *30*(12), 1643. https://doi.org/10.1029/2003GL016974

Hensen, C., Nuzzo, M., Hornibrook, E., Pinheiro, L. M., Bock, B., Magalhães, V. H., & Brückmann, W. (2007). Sources of mud volcano fluids in the Gulf of Cadiz—Indications for hydrothermal imprint. *Geochimica et Cosmochimica Acta*, *71*(5), 1232–1248. https://doi.org/10.1016/j.gca.2006.11.022

Hensen, C., Wallmann, K., Schmidt, M., Ranero, C. R., & Suess, E. (2004). Fluid expulsion related to mud extrusion off Costa Rica—A window to the subducting slab. *Geology*, *32*(3), 201–204. https://doi.org/10.1130/G20119.1

Horai, K.-I. (1971). Thermal conductivity of rock-forming minerals. *Journal of Geophysical Research*, *76*(5), 1278–1308. https://doi.org/10.1029/JB076i005p01278

Horai, K.-I., & Simmons, G. (1969). Thermal conductivity of rock-forming minerals. *Earth and Planetary Science Letters*, *6*(5), 359–368. https://doi.org/10.1016/0012-821X(69)90186-1

Hovland, M., Svensen, H., Forsberg, C. F., Johansen, H., Fichler, C., Fosså, J. H., et al. (2005). Complex pockmarks with carbonate-ridges off mid-Norway: Products of sediment degassing. *Marine Geology*, *218*(1-4), 191–206. https://doi.org/10.1016/j.margeo.2005.04.005

Jang, J., & Santamarina, J. C. (2014). Evolution of gas saturation and relative permeability during gas production from hydrate-bearing sediments: Gas invasion vs. gas nucleation. *Journal of Geophysical Research: Solid Earth*, *119*, 116–126. https://doi.org/10.1002/2013JB010480

Juanes, R., & Bryant, S. L. (2006). Mechanisms leading to co-existence of gas and hydrate in ocean sediments. (U.S. Department of Energy, 2006).

Kamath, V. A. (1984). Study of heat transfer characteristics during dissociation of gas hydrates in porous media (Doctoral dissertation). Pennsylvania (USA): University of Pittsburgh.

Kannberg, P. K., Tréhu, A. M., Pierce, S. D., Paull, C. K., & Caress, D. W. (2013). Temporal variation of methane flares in the ocean above Hydrate Ridge, Oregon. *Earth and Planetary Science Letters*, *368*, 33–42. https://doi.org/10.1016/j.epsl.2013.02.030

Kim, J.-H., Torres, M. E., Hong, W.-L., Choi, J., Riedel, M., Bahk, J.-J., & Kim, S.-H. (2013). Pore fluid chemistry from the Second Gas Hydrate Drilling Expedition in the Ulleung Basin (UBGH2): Source, mechanisms and consequences of fluid freshening in the central part of the Ulleung Basin, East Sea. *Marine and Petroleum Geology*, *47*, 99–112. https://doi.org/10.1016/j.marpetgeo.2012.12.011

Klaucke, I., Sahling, H., Weinrebe, W., Blinova, V., Bürk, D., Lursmanashvili, N., & Bohrmann, G. (2006). Acoustic investigation of cold seeps offshore Georgia, eastern Black Sea. *Marine Geology*, *231*(1-4), 51–67. https://doi.org/10.1016/j.margeo.2006.05.011

Koch, S., Berndt, C., Bialas, J., Haeckel, M., Crutchley, G., Papenberg, C., et al. (2015). Gas-controlled seafloor doming. *Geology*, *43*(7), 571–574. https://doi.org/10.1130/G36596.1

Koch, S., Schroeder, H., Haeckel, M., Berndt, C., Bialas, J., Papenberg, C., et al. (2016). Gas migration through Opouawe Bank at the Hikurangi margin offshore New Zealand. *Geo-Marine Letters*, *36*(3), 187–196. https://doi.org/10.1007/s00367-016-0441-y

Kossel, E., Deusner, C., Bigalke, N., & Haeckel, M. (2018). The dependence of water permeability in quartz sand on gas hydrate saturation in the pore space. *Journal of Geophysical Research: Solid Earth*, *123*(2), 1235–1251. https://doi.org/10.1002/2017JB014630

Kulm, L., Suess, E., Moore, J., Carson, B., Lewis, B., Ritger, S., et al. (1986). Oregon subduction zone: Venting, fauna, and carbonates. *Science*, *231*(4738), 561–566. https://doi.org/10.1126/science.231.4738.561

Law, C., Nodder, S. D., Mountjoy, J., Marriner, A., Orpin, A., Pilditch, C. A., et al. (2010). Geological, hydrodynamic and biogeochemical variability of a New Zealand deep-water methane cold seep during an integrated three-year time-series study. *Marine Geology*, *272*(1–4), 189–208. https://doi.org/10.1016/j.margeo.2009.06.018

Leung, C., Hoch, A., & Zimmerman, R. (2012). Comparison of discrete fracture network and equivalent continuum simulations of fluid flow through two-dimensional fracture networks for the DECOVALEX–2011 project. *Mineralogical Magazine*, *76*(8), 3179–3190. https://doi.org/10.1180/minmag.2012.076.8.31

Li, B., Li, X.-S., & Li, G. (2014). Kinetic studies of methane hydrate formation in porous media based on experiments in a pilot-scale hydrate simulator and a new model. *Chemical Engineering Science*, *105*, 220–230. https://doi.org/10.1016/j.ces.2013.11.016

Liu, X., & Flemings, P. B. (2006). Passing gas through the hydrate stability zone at southern Hydrate Ridge, offshore Oregon. *Earth and Planetary Science Letters*, *241*(1-2), 211–226. https://doi.org/10.1016/j.epsl.2005.10.026

Liu, X., & Flemings, P. B. (2007). Dynamic multiphase flow model of hydrate formation in marine sediments. *Journal of Geophysical Research*, *112*, B03101. https://doi.org/10.1029/2005JB004227

Liu, X., & Flemings, P. B. (2011). Capillary effects on hydrate stability in marine sediments. *Journal of Geophysical Research*, *116*, B07102. https://doi.org/10.1029/2010JB008143

Locat, J., & Lee, H. J. (2002). Submarine landslides: Advances and challenges. *Canadian Geotechnical Journal*, *39*(1), 193–212. https://doi.org/10.1139/t01-089

Mahabadi, N., Dai, S., Seol, Y., Sup Yun, T., & Jang, J. (2016). The water retention curve and relative permeability for gas production from hydrate-bearing sediments: Pore-network model simulation. *Geochemistry, Geophysics, Geosystems*, *17*, 3099–3110. https://doi.org/10.1002/2016GC006372

Mahabadi, N., & Jang, J. (2014). Relative water and gas permeability for gas production from hydrate-bearing sediments. *Geochemistry, Geophysics, Geosystems*, *15*, 2346–2353. https://doi.org/10.1002/2014GC005331

Matsumoto, R., Kakuwa, Y., Snyder, G., Tanahashi, M., Hiruta, A., Oi, T., et al. 2017). Occurrence and origin of thick deposits of massive gas hydrate, eastern margin of the Sea of Japan. Paper presented at 9th International Conference on Gas Hydrates (ICGH9), Denver, CO.

Matsumoto, R., Tanahashi, M., Kakuwa, Y., Snyder, G., Ohkawa, S., Tomaru, H., & Morita, S. (2017). Recovery of thick deposits of massive gas hydrates from gas chimney structures, eastern margin of Japan Sea: Japan Sea Shallow Gas Hydrate Project. *Fire in the Ice*, *17*(1), 1–6.

Milkov, A. V., Claypool, G. E., Lee, Y.-J., & Sassen, R. (2005). Gas hydrate systems at Hydrate Ridge offshore Oregon inferred from molecular and isotopic properties of hydrate-bound and void gases. *Geochimica et Cosmochimica Acta*, *69*(4), 1007–1026. https://doi.org/10.1016/j.gca.2004.08.021

Milkov, A. V., Dickens, G. R., Claypool, G. E., Lee, Y.-J., Borowski, W. S., Torres, M. E., et al. (2004). Co-existence of gas hydrate, free gas, and brine within the regional gas hydrate stability zone at Hydrate Ridge (Oregon margin): Evidence from prolonged degassing of a pressurized core. *Earth and Planetary Science Letters*, *222*(3-4), 829–843. https://doi.org/10.1016/j.epsl.2004.03.028

Mohebbi, V., Naderifar, A., Behbahani, R., & Moshfeghian, M. (2012). Investigation of kinetics of methane hydrate formation during isobaric and isochoric processes in an agitated reactor. *Chemical Engineering Science*, *76*, 58–65. https://doi.org/10.1016/j.ces.2012.04.016

Moridis, G. J., Kowalsky, M. B., & Pruess, K. (2008). TOUGH+HYDRATE v1.0 user's manual: A code for the simulation of system behavior in hydrate-bearing geologic media. (Rep. LBNL-149E). Berkeley, CA: Lawrence Berkeley National Laboratory.

Naudts, L., Greinert, J., Artemov, Y., Staelens, P., Poort, J., Van Rensbergen, P., & De Batist, M. (2006). Geological and morphological setting of 2778 methane seeps in the Dnepr paleo-delta, northwestern Black Sea. *Marine Geology*, *227*(3-4), 177–199. https://doi.org/10.1016/j.margeo.2005.10.005

Neuzil, C. (1994). How permeable are clays and shales? *Water Resources Research*, *30*(2), 145–150. https://doi.org/10.1029/93WR02930

Nimblett, J., & Ruppel, C. (2003). Permeability evolution during the formation of gas hydrates in marine sediments. *Journal of Geophysical Research*, *108*(B9), 2420. https://doi.org/10.1029/2001JB001650

Olu, K., Lance, S., Sibuet, M., Henry, P., Fiala-Médioni, A., & Dinet, A. (1997). Cold seep communities as indicators of fluid expulsion patterns through mud volcanoes seaward of the Barbados accretionary prism. *Deep Sea Research Part I: Oceanographic Research Papers*, *44*(5), 811–841. https://doi.org/10.1016/S0967-0637(96)00123-9

Paull, C. K., Matsumoto, R., Wallace, P., Black, N. R., Borowski, W. S., Collett, T. S., et al. (1996). *Proc. ODP*, Init. Repts. (Vol. 164). College Station, TX: Ocean Drilling Program. https://doi.org/10.2973/odp.proc.ir.164.1996, http://www-odp.tamu.edu/publications/164_IR/VOLUME/CHAPTERS/164ir.pdf

Pruess, K., & Tsang, Y. W. (1990). On two-phase relative permeability and capillary pressure of rough-walled rock fractures. *Water Resources Research*, *26*(9), 1915–1926. https://doi.org/10.1029/WR026i009p01915

Reilly, M. J., & Flemings, P. B. (2010). Deep pore pressures and seafloor venting in the Auger Basin, Gulf of Mexico. *Basin Research*, *22*(4), 380–397. https://doi.org/10.1111/j.1365-2117.2010.00481.x

Reitz, A., Haeckel, M., Wallmann, K., Hensen, C., & Heeschen, K. (2007). Origin of salt-enriched pore fluids in the northern Gulf of Mexico. *Earth and Planetary Science Letters*, *259*(3-4), 266–282. https://doi.org/10.1016/j.epsl.2007.04.037

Reitz, A., Pape, T., Haeckel, M., Schmidt, M., Berner, U., Scholz, F., et al. (2011). Sources of fluids and gases expelled at cold seeps offshore Georgia, eastern Black Sea. *Geochimica et Cosmochimica Acta*, *75*(11), 3250–3268. https://doi.org/10.1016/j.gca.2011.03.018

Riedel, M., Collett, T. S., Malone, M. J., & the Expedition 311 Scientists (2006). *Proc. IODP* (Vol. 311). Washington, DC: Integrated Ocean Drilling Program Management International, Inc. https://doi.org/10.2204/iodp.proc.311.2006

Riedel, M., Spence, G., Chapman, N., & Hyndman, R. (2002). Seismic investigations of a vent field associated with gas hydrates, offshore Vancouver Island. *Journal of Geophysical Research*, *107*(B9), EPM 5-1–EPM 5-16. https://doi.org/10.1029/2001JB000269

Römer, M., Sahling, H., Pape, T., Bahr, A., Feseker, T., Wintersteller, P., & Bohrmann, G. (2012). Geological control and magnitude of methane ebullition from a high-flux seep area in the Black Sea—The Kerch seep area. *Marine Geology*, *319-322*, 57–74. https://doi.org/10.1016/j.margeo.2012.07.005

Ruppel, C., Dickens, G., Castellini, D., Gilhooly, W., & Lizarralde, D. (2005). Heat and salt inhibition of gas hydrate formation in the northern Gulf of Mexico. *Geophysical Research Letters*, *32*, L04605. https://doi.org/10.1029/2004GL021909

Rutqvist, J., & Moridis, G. J. (2009). Numerical studies on the geomechanical stability of hydrate-bearing sediments. *SPE Journal*, *SPE-126129-PA*, *14*(02), 267–282. https://doi.org/10.2118/126129-PA

Skovborg, P., & Rasmussen, P. (1994). A mass transport limited model for the growth of methane and ethane gas hydrates. *Chemical Engineering Science*, *49*(8), 1131–1143. https://doi.org/10.1016/0009-2509(94)85085-2

Smith, A. J., Flemings, P. B., Liu, X., & Darnell, K. (2014). The evolution of methane vents that pierce the hydrate stability zone in the world's oceans. *Journal of Geophysical Research: Solid Earth*, *119*, 6337–6356. https://doi.org/10.1002/2013JB010686

Smith, A. J., Mienert, J., Bünz, S., & Greinert, J. (2014). Thermogenic methane injection via bubble transport into the upper Arctic Ocean from the hydrate-charged Vestnesa Ridge, Svalbard. *Geochemistry, Geophysics, Geosystems*, *15*, 1945–1959. https://doi.org/10.1002/2013GC005179

Snow, D. T. (1968). Rock fracture spacings, openings, and porosities. *Journal of the Soil Mechanics and Foundations Division*, *94*(1), 73–92.

Spiteri, E. J., Juanes, R., Blunt, M. J., & Orr, F. M. (2008). A new model of trapping and relative permeability hysteresis for all wettability characteristics. *SPE Journal*, *SPE-96448-PA*, *13*(03), 277–288. https://doi.org/10.2118/96448-PA

Stone, H. L. (1970). Probability model for estimating three-phase relative permeability. *Journal of Petroleum Technology*, *22*(02), 214–218. https://doi.org/10.2118/2116-PA

Suess, E., Torres, M. E., Bohrmann, G., Collier, R., Greinert, J., Linke, P., et al. (1999). Gas hydrate destabilization: enhanced dewatering, benthic material turnover and large methane plumes at the Cascadia convergent margin. *Earth and Planetary Science Letters*, *170*(1-2), 1–15. https://doi.org/10.1016/S0012-821X(99)00092-8

Torres, M. E., Wallmann, K., Tréhu, A., Bohrmann, G., Borowski, W., & Tomaru, H. (2004). Gas hydrate growth, methane transport, and chloride enrichment at the southern summit of Hydrate Ridge, Cascadia margin off Oregon. *Earth and Planetary Science Letters*, *226*(1-2), 225–241. https://doi.org/10.1016/j.epsl.2004.07.029

Tréhu, A. M., Bohrmann, G., Rack, F. R., Torres, M. E., Bangs, N. L., Barr, S. R., et al. (2003). *Proc. ODP, Init. Repts.* (Vol. 204). College Station, TX: Ocean Drilling Program. https://doi.org/10.2973/odp.proc.ir.204.2003, http://www-odp.tamu.edu/publications/204_IR/204IR.PDF

Tréhu, A. M., Flemings, P. B., Bangs, N. L., Chevallier, J., Gràcia, E., Johnson, J. E., et al. (2004). Feeding methane vents and gas hydrate deposits at south Hydrate Ridge. *Geophysical Research Letters*, *31*, L23310. https://doi.org/10.1029/2004GL021286

Tréhu, A. M., Long, P. E., Torres, M. E., Bohrmann, G., Rack, F., Collett, T. S., et al. (2004). Three-dimensional distribution of gas hydrate beneath southern Hydrate Ridge: Constraints from ODP Leg 204. *Earth and Planetary Science Letters*, *222*(3-4), 845–862. https://doi.org/10.1016/j.epsl.2004.03.035

Van Genuchten, M. T. (1980). A closed-form equation for predicting the hydraulic conductivity of unsaturated soils. *Soil Science Society of America Journal*, *44*(5), 892–898. https://doi.org/10.2136/sssaj1980.03615995004400050002x

Wallmann, K., Drews, M., Aloisi, G., & Bohrmann, G. (2006). Methane discharge into the Black Sea and the global ocean via fluid flow through submarine mud volcanoes. *Earth and Planetary Science Letters*, *248*(1-2), 545–560. https://doi.org/10.1016/j.epsl.2006.06.026

Weinberger, J. L., & Brown, K. M. (2006). Fracture networks and hydrate distribution at Hydrate Ridge, Oregon. *Earth and Planetary Science Letters*, *245*(1-2), 123–136. https://doi.org/10.1016/j.epsl.2006.03.012

Whelan, T. III, Coleman, J., Suhayda, J., & Roberts, H. (1977). Acoustical penetration and shear strength in gas-charged sediment. *Marine Georesources & Geotechnology*, *2*(1-4), 147–159. https://doi.org/10.1080/10641197709379776

Xu, Y., Seol, Y., Jang, J., & Dai, S. (2017). Water and Gas Flows in Hydrate-Bearing Sediments. Paper presented at Geotechnical Frontiers 2017, GSP 280, 766–772.

Zimmerman, R. W., & Bodvarsson, G. S. (1996). Hydraulic conductivity of rock fractures. *Transport in Porous Media*, *23*(1), 1–30. https://doi.org/10.1007/BF00145263

Zühlsdorff, L., & Spiess, V. (2004). Three-dimensional seismic characterization of a venting site reveals compelling indications of natural hydraulic fracturing. *Geology*, *32*(2), 101–104. https://doi.org/10.1130/G19993.1